Surface heat flux variability over the northern California shelf

Robert C. Beardsley
Department of Physical Oceanography, Woods Hole Oceanographic Institution
Woods Hole, Massachusetts

Edward P. Dever
Center for Coastal Studies, Scripps Institution of Oceanography
University of California, San Diego, La Jolla

Steven J. Lentz and Jerome P. Dean
Department of Physical Oceanography, Woods Hole Oceanographic Institution
Woods Hole, Massachusetts

Abstract. Surface heat flux components are estimated at a midshelf site over the northern California shelf using moored measurements from the 1981–1982 Coastal Ocean Dynamics Experiment (CODE) and the 1988–1989 Shelf Mixed Layer Experiment (SMILE). Time series of estimated fluxes extend from early winter through summer upwelling conditions, allowing examination of seasonal variations as well as synoptic events. On a seasonal timescale, the surface heat flux is strongly influenced net surface heat flux are the annual variation in incident shortwave solar radiation (insolation) and the atmospheric spring transition. Between mid-November 1988 and late February 1989, insolation is weak and the mean daily averaged heat flux is nearly zero (absolute value less than 10 W m^{-2}), with a standard deviation of ~50 W m^{-2}. Beginning in March, insolation increases markedly, and typical daily-averaged heat fluxes increase to greater than 100 W m^{-2} by the spring transition in April or May. In June and July, the average heat flux is near 200 W m^{-2}, with a standard deviation of ~90 W m^{-2}. In winter, the daily-averaged heat flux varies on periods of several days. Net heat flux losses can range up to 130 W m^{-2}. These losses are not identified with any one type of event. For example, comparable heat flux losses can occur for very low relative humidities (*RHs*), moderate winds, and clear skies, and for high *RHs*, high winds, and cloudy skies. In summer, surface heat flux variability is strongly influenced by upwelling and relaxation events. Upwelling is characterized by clear skies and high equatorward winds, while relaxation is characterized by the presence of clouds and low or northward winds. These conditions lead to opposing changes in insolation and in longwave radiative cooling and latent heat flux. Variability in insolation dominates, and the daily-averaged heat flux into the ocean is greatest during upwelling events (up to 350 W m^{-2} or more) and least during relaxation events (sometimes less than 100 W m^{-2}).

1. Introduction

It has been well known since the pioneering coastal upwelling experiments conducted in the 1970s that atmospheric surface forcing (i.e., wind stress and heat flux) can strongly influence vertical mixing, stratification, and currents over the continental shelf [e.g.,

Halpern, 1976]. The Coastal Ocean Dynamics Experiment (CODE) was conducted over the northern California shelf during spring–summer 1981 and 1982 in part to understand the response of the coastal ocean to strong local surface forcing (i.e., persistent upwelling-favorable winds and large positive heat flux) during the coastal upwelling season [*Beardsley and Lentz*, 1987]. The Shelf Mixed Layer Experiment (SMILE) was conducted in the same area during 1988–1989 to study the coastal ocean surface boundary layer response to the more variable atmospheric forcing which characterizes
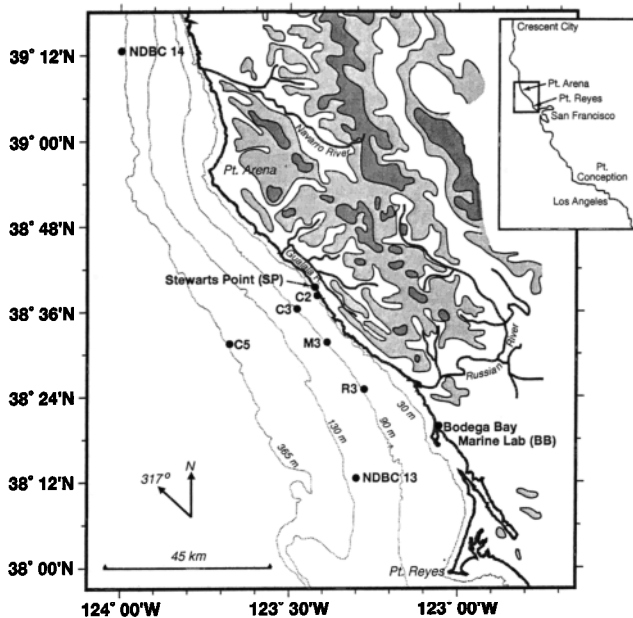
Figure 1. Map of CODE and SMILE region between Point Reyes and Point Arena, showing the midshelf site C3 where the surface heat flux was estimated from moored measurements and other sites providing data used in this study. NDBC13 and NDBC14 denote NOAA Data Buoy Center environmental buoys 44014 and 44013. The coastal mountain range is shown shaded, with lightly and heavily areas representing elevations greater than 305 m and 610 m, respectively.

winter off northern California [*Alessi et al.*, 1991; *Dever*, 1997].

In both CODE and SMILE, atmospheric and oceanographic variables were measured at a midshelf site (denoted C3 in Figure 1) to allow estimation of surface forcing. The resultant surface heat flux time series have been used by different investigators to study a variety of dynamical processes over the northern California shelf. For example, *Rudnick and Davis* [1988] and *Lentz* [1987a] have shown that the surface heat flux becomes important in summer to the shelf volume heat budget on timescales of about one month or more, although it is small compared to advective fluxes on event timescales of days to weeks. Similarly, *Dever and Lentz* [1994] showed that the surface heat flux is important to the mean heat balance in spring. The surface heat flux also influences the character of the oceanic surface boundary layer. *Brink* [1983] and *Rosenfeld* [1987] found evidence that the surface heat flux can modify diurnal variability in the surface mixed layer in coastal upwelling regions. On subtidal timescales, *Lentz* [1992] found that the magnitude of a positive surface heat flux did not strongly influence surface mixed layer depth during active upwelling, a fact he attributed to a balance between surface heating and offshore advection. This agrees with the *Federiuk and Allen* [1995] model study of summer upwelling circulation off Oregon which found the surface boundary layer structure was relatively insensitive

to a doubling of the surface heat flux from the base case examined. However, the same study also found the presence of surface heating was important in that surface heating greatly reduced the depth of the surface boundary layer compared to a no-surface-heating case. During SMILE, the surface mixed layer deepens in response to the winter surface cooling discussed here.

The spring transition to upwelling occurred in late March before Code 1 (mid-April through July 1981) and in mid-April during Code 2 (late March through July 1982), so both observation periods include much of the upwelling season. SMILE (mid-November 1988 through mid-May 1989) covered winter and the subsequent spring transition. Taken together, the CODE and SMILE measurement periods cover all but fall, suggesting that a careful analysis of the C3 heat flux time series should provide a good comparison with existing climatology and new insight into heat flux variability on shorter timescales, especially those associated with synoptic weather events which characterize the northern California shelf.

This paper is organized as follows. The basic formulas used to estimate heat flux from moored data are presented next (section 2), followed by brief descriptions of the moored instrumentation used in CODE and SMILE, measurement uncertainty, and hourly time series of the basic variables measured at C3 (section 3). The C3 daily-averaged heat flux time series are presented next (section 4), followed by a detailed look at the influence of synoptic weather events on the C3 heat flux (section 5). The spatial variability of some heat flux components is summarized next (section 6), followed by a comparison of the C3 monthly-averaged heat flux time series with the monthly mean climatology of *Nelson and Husby* [1983] (section 7) and a summary and conclusions (section 8). Appendix A presents a discussion of measurement problems and solutions, and Appendix B presents a time series of surface heat flux estimated from moored measurements obtained on the Oregon shelf during summer 1972.

2. Estimation of Surface Heat Flux From Moored Data

The net surface heat flux Q_n into the ocean is the sum of four components

$$Q_n = Q_i + Q_b + Q_s + Q_l, \qquad (1)$$

where Q_i and Q_b are the net incident shortwave and longwave radiation fluxes, Q_s the sensible heat flux due to air–sea temperature difference, and Q_l the latent heat flux due to water vapor transport. Here, positive flux values indicate flux into the ocean. The following formulas were used to estimate these components from hourly averaged moored data.

Shortwave heat flux was estimated by

$$Q_i = (1 - A_b)I_{sw}, \qquad (2)$$

where A_b is the ocean albedo indicating the fraction of the measured insolation I_{sw} which is reflected or scattered upward at the ocean surface. *Payne* [1972] showed that A_b depends primarily on the solar altitude and atmospheric transmittance T_r, and to a much lesser extent the surface roughness. Using software developed by R. Payne (personal communication, 1996), we first computed the instantaneous solar altitude and the no-sky insolation, I_{swns} and then computed $T_r = I_{sw}/I_{swns}$ and interpolated hourly values of A_b using Table 1 of *Payne* [1972]. Typical albedos over the northern California shelf ranged from 0.08–0.10 in winter to 0.05–0.07 in summer. Note that use of an accurate A_b reduces the uncertainty in Q_i to essentially that in the I_{sw} measurement.

Longwave heat flux was estimated from measured downward longwave and shortwave radiation and grey body upward radiation during SMILE and from a formula derived from daily-averaged cloud cover during CODE 1 and CODE 2. During SMILE, longwave heat flux was computed using

$$Q_b = \epsilon\left((I_{lw} - 0.036I_{sw}) - \sigma T_s^4 \right), \qquad (3)$$

where I_{lw} is the measured downward longwave radiation, the second term is a correction for solar heating of the longwave sensor using I_{sw} and a constant coefficient of proportionality [*Alados-Arboledas et al.*, 1988; *Dickey et al.*, 1994], ϵ is the emissivity of the ocean surface (taken as 0.98 [*Dickey et al.*, 1994]), σ is the Stefan-Boltzmann constant, and T_s is the surface temperature in degrees Kelvin.

During CODE, incident longwave radiation was not measured, and we employed a bulk formula to estimate Q_b. *Fung et al.* [1984] compared eight commonly used bulk formulas for Q_b against the results of a full radiative transfer model, and found that while some formulas estimated Q_b to within ± 15 W m^{-2} under clear sky conditions, the differences were much greater during cloudy conditions. To determine the best formula to use during CODE, the eight formulas were used to estimate a bulk Q_b during SMILE which was then compared to (3).

These comparisons showed that a modified version of the *Berliand and Berliand* [1952] formula provided the best fit, with the original quadratic cloud correction factor $(1 - bC^2)$ replaced by the linear expression $(1 - bC)$, where b was chosen to minimize the least squares difference between the daily averaged bulk Q_b and (3). The net longwave heat flux was thus estimated using

$$Q_b = \left(\epsilon\sigma T_s^4(0.39 - 0.05e^{0.5}) + 4\epsilon\sigma T_s^3(T_s - T_a) \right)(1 - b\overline{C}), \qquad (4)$$

where e is the vapor pressure, T_a is the (absolute) air temperature, and $b = 0.75$. The daily-averaged cloud

cover $\overline{C}$ was estimated using the *Reed* [1976] formula

$$\overline{C} = \left(1 - (\overline{I}_{sw}/\overline{I}_{swcs}) + .0019\alpha \right)/0.62, \qquad (5)$$

where $\overline{I}_{sw}$ is the measured daily mean insolation, $\overline{I}_{swcs}$ is the daily average clear sky insolation, and α is the local noon solar altitude. Both $\overline{I}_{swcs}$ and α were computed using the Smithsonian meteorological tables [*List*, 1984]. Following *Reed* [1976], cloud covers less than 0.3 were set to zero in (4). In SMILE, the difference in the daily-averaged bulk Q_b computed using (4) and (5) and the measured Q_b given by (3) is -1.4 ± 13.8 W m^{-2}. The difference de-correlation timescale is about two days, so that the impact of maximum differences of order ±40 W m^{-2} diminish on timescales of a few weeks.

Sensible and latent heat fluxes were estimated from

$$Q_s = \rho c_p C_h(T_a - T_s)U, \qquad (6)$$

and

$$Q_l = \rho L_e C_e(q_a - 0.98q_{sat})U, \qquad (7)$$

where ρ is the air density, c_p is the heat capacity of air, C_h the sensible heat flux transfer coefficient, U is the magnitude of the measured wind velocity minus the surface current velocity (i.e., $U = |\mathbf{U}_a - \mathbf{U}_s|$), L_e is the latent heat of evaporation of seawater, C_e is the latent heat flux transfer coefficient, q_a is the specific humidity (computed using the measured relative humidity RH and T_a), and 0.98 q_{sat} is the specific humidity just above the sea surface (where RH is assumed to be 98% above salt water). Since the measured wind velocities were generally much larger than the near-surface currents, we show wind velocity only to simplify the data presentation. The near-surface current time series used in the heat flux calculations are shown by *Rosenfeld* [1983], *Limeburner* [1985], and *Alessi et al.* [1991].

The sensible and latent heat flux transfer coefficients C_h and C_e used in (6) and (7) were computed using the Tropical Ocean–Global Atmosphere/Coupled Ocean–Atmosphere Response Experiment (TOGA/COARE) bulk formulation [*Fairall et al.*, 1996] without correction for skin temperature effects. This code, based on the stability-dependent bulk approach of *Liu et al.* [1979] and neutral 10-m drag coefficient of *Smith* [1988], was developed for application to the tropical Pacific and incorporates increased heat fluxes due to gustiness at low wind speeds.

It is an open question how well this (or any other open ocean) code estimates turbulent air–sea fluxes over the continental shelf where large spatial and temporal changes in surface conditions (such as aerodynamic roughness and temperature) can occur. While this point will be discussed more in section 4.3, results summarized by *Fairall and Markson* [1987] and *Garratt* [1990] suggest that our atmospheric measurements were made sufficiently close to the ocean sur-

Table 1. Moored and Coastal Stations

Experiment Name	Site	Latitude °N	Longitude °W	Water Depth m	Variables Measured
CODE 1	C3	38.61	123.47	94	U_a, I_{sw}, T_a, T_s, U_s
	C5	38.52	123.67	402	U_a, I_{sw}, T_a, T_s, U_s
	NDBC13	38.20	123.30	125	P_a
	NDBC14	39.20	124.00	306	P_a
CODE 2	C3	38.61	123.46	93	U_a, I_{sw}, RH, P_a, T_a, T_s, U_s
	C2	38.64	123.42	59	I_{sw}
	C5	38.51	123.67	400	P_a
	R3	38.42	123.27	90	I_{sw}
	NDBC13	38.20	123.30	125	P_a
	NDBC14	39.20	124.00	306	P_a
SMILE	C3	38.65	123.49	93	U_a, I_{sw}, I_{lw}, RH, P_a, T_a, T_s, U_s
	M3	38.54	123.38	93	T_s
	NDBC13	38.20	123.30	125	T_a
	NDBC14	39.20	124.00	306	T_a
	SP	38.66	123.40	28*	I_{sw}, I_{lw}
	BB	38.32	123.07	9*	I_{sw}

Moored and coastal stations which provided primary and secondary data to estimate the surface heat flux in CODE and SMILE are listed. The two coastal stations at Stewarts Point and the Bodega Bay Marine Laboratory are denoted by SP and BB, respectively. The right-hand column lists the variables measured at each station: vector wind (U_a), insolation (I_{sw}), incident longwave flux (I_{lw}), air pressure (P_a), relative humidity (RH), air temperature (T_a), water temperature (T_s) and ocean current (U_s).

*Sensor heights above sea level.

face that bulk formulations should provide good estimates of the turbulent air-sea fluxes, even during stable conditions when the atmospheric boundary layer tends to be thinner. For the northern California shelf, the heat and momentum fluxes computed using the TOGA/COARE code agree closely with those calculated using the Large and Pond [1981,1982](LP) bulk formulation. In SMILE, aircraft-measured wind stresses agree on average within 0.01 ± 0.02 N m^{-2} with buoy wind stresses estimated using both TOGA/COARE and LP codes [Beardsley et al., 1997], and aircraft-based estimates of the 10-m neutral transfer coefficients C_h and C_e agree within uncertainty with the values used in both TOGA/COARE and LP [Enriquez and Friehe, 1997]. (The MATLAB programs used here to compute the surface fluxes may be found on the worldwide web at http://crusty.er.usgs.gov/sea-mat.)

3. C3 Moored Measurements

Calculation of Q_n using the above formulas requires moored measurements of wind and ocean surface velocities U_a and U_s, the air and ocean surface temperatures T_a and T_s, insolation I_{sw}, relative humidity RH, barometric pressure P_a, and (for direct estimates of Q_b) downward longwave radiation I_{lw}. Unfortunately, not all these variables were successfully measured at C3 in the different field programs; Table 1 identifies the different moored and coastal sites where measurements used

in this study were obtained, and Appendix A presents the methods and assumptions used to construct complete hourly time series of the basic variables listed above at C3 for each experiment. The moored instrumentation used in CODE and SMILE and their experimental uncertainties are summarized next, followed by a description of the C3 time series. Additional information about the field programs is presented by Rosenfeld [1983], Limeburner [1985], and Alessi et al. [1991].

Moored Instrumentation

The Woods Hole Oceanographic Institution (WHOI) vector-averaging wind recorder (VAWR) served as the basic meteorological sensing and recording system in CODE and SMILE [Dean and Beardsley, 1988; Trask et al., 1989]. Mounted on a 3-m toroid buoy, the Code 1 VAWR measured wind speed and direction, insolation, air temperature, and water temperature. In Code 2, air pressure and RH sensors were added (Figure 2a). In SMILE, two integral VAWRs were mounted on a 3.5-m discus buoy at C3 to provide wind measurements at several heights and provide redundant measurements of other variables, including downward longwave radiation and improved RH sensors (Figure 2b). Near-surface ocean currents and temperature were measured at C3 in all experiments with either Scripps Institution of Oceanography (SIO) or vector-measuring current meters (VMCMs) [Weller and Davis, 1980; Beard-
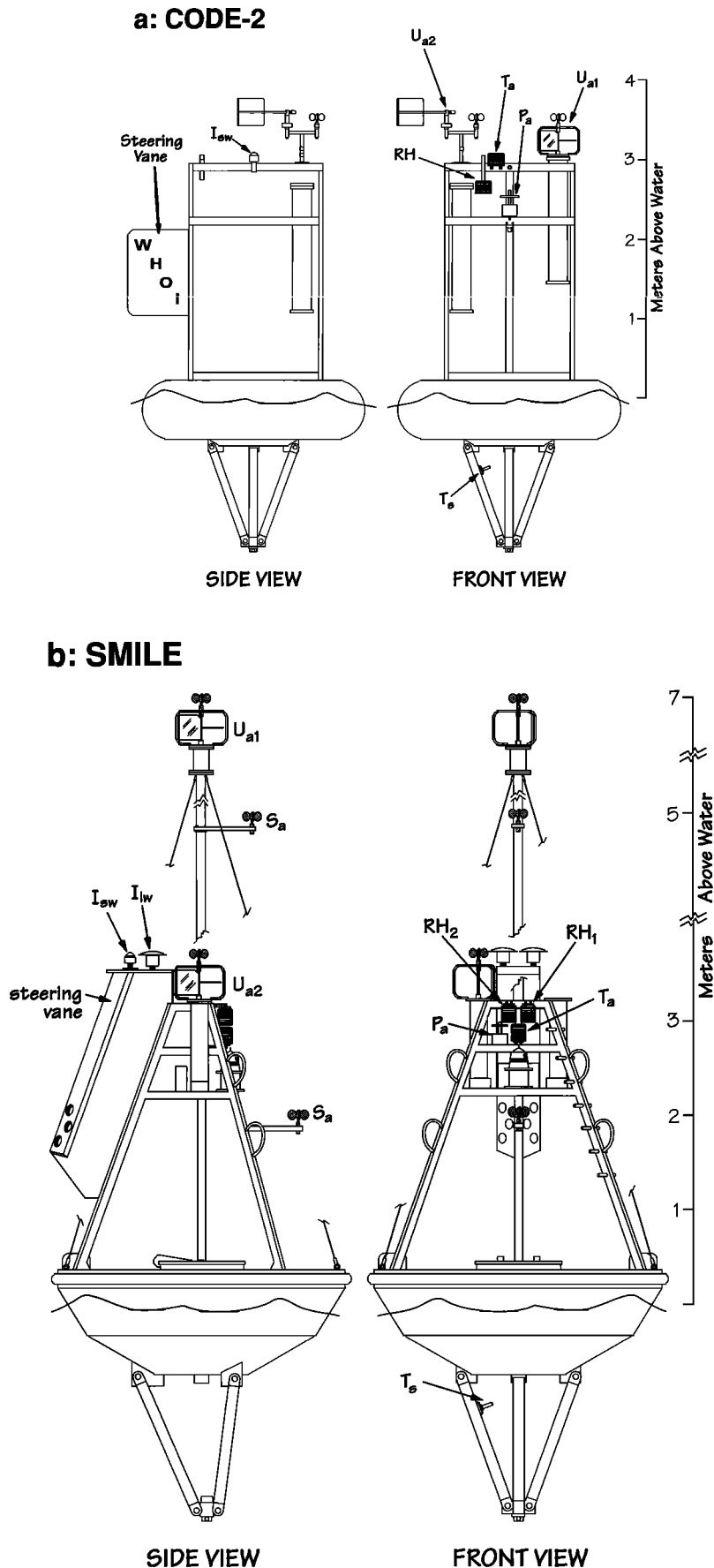
a: CODE-2

SIDE VIEW   FRONT VIEW

b: SMILE

SIDE VIEW   FRONT VIEW

Figure 2. Schematics of the meteorological buoys deployed at C3 in (a) CODE 2 and (b) SMILE. The CODE 1 C3 buoy was identical in design to CODE 2 but lacked air pressure and RH sensors. All C3 buoys had steering vanes to help orient the meteorological sensors into the wind.

Table 2. C3 Sensor Heights Above Water During Each Experiment

Variable	CODE 1	CODE 2	SMILE
Wind speed, wind direction	3.5	3.5	3.5
Current speed, direction	−5.0	−5.0	−5.5
Insolation	3.0	3.0	3.5
Longwave	...	...	3.5
Air pressure	...	2.5	2.7
Relative humidity	...	2.7	3.0
Air temperature	3.0	3.0	10.0
Water temperature	−1.0	−1.0	−6.0
Platform	toroid	toroid	discus

The C5 sensor heights during CODE-1 were identical to the C3 buoy. The SMILE air temperature height is that at NDBC13. The SMILE C3 water temperature at 6 m is adjusted by the near-surface (1–5 m) temperature difference at M3, 15 km south of C3. (See Appendix A for details).

sley, 1987]. Table 2 lists the C3 sensor heights for each experiment.

Table 3 summarizes by instrument and variable the different sensors used in CODE and SMILE and estimates of their in situ measurement uncertainty. This uncertainty includes the inherent sensor error, the system error introduced between the sensor output and the recorded digital value, and any additional error caused by unsteadiness in the marine layer, mooring motion, poor sensor placement, imperfect protection of different sensors from solar heating, etc. The contribution of these in situ measurement uncertainties plus other measurement problems (Appendix A) to the uncertainties in the computed heat flux components is discussed in section 4.

C3 Meteorological Time Series

The C3 hourly meteorological time series from SMILE (Figure 3), CODE 2 (Figure 4) and CODE 1 (Figure 5) provide insight into the causes of temporal surface heat flux variability. These records cover the following periods: SMILE (0800 UT, November 14, 1988 to 0700 UT, May 14, 1989); CODE 1 (0800 UT, April 13, 1981 to 0700 UT, July 31, 1981); and CODE 2 (0800 UT, March 25, 1982 to 0700 UT, July 28, 1982). These and subsequent time series are plotted using UT, where UT = local (Pacific Standard) time + 8 hours. An on-shelf and along-shelf coordinate system is used to display the vector wind, with the positive on-shelf u component oriented toward 47°and the positive along-shelf v component directed toward 317°.

Taken together, the SMILE and CODE field programs span most of the year, and seasonal trends in most of the basic variables are evident. While I_{sw} and T_a reach their maxima in summer months, the seasonal cycle of wind forcing [_Strub et al._, 1987] affects T_s. Following the atmospheric spring transition [_Lentz_, 1987b], strong ($v < -10$ m s^{-1}) persistent equatorward along-

shelf winds drive coastal upwelling. This reduces T_s during summer so that trends in T_s and T_a oppose each other. In summer, T_s is generally less than T_a (leading to a stable atmospheric marine layer), while in winter, when the along-shelf winds are generally weaker and more variable, T_a is generally less than the prevailing T_s (leading to an unstable marine layer).

The C3 time series also demonstrate strong variability on diurnal and synoptic (2–10-day) timescales. Much of this variability is not independent. In all seasons, there is a link between wind direction and cloud cover. Equatorward winds are often associated with clear skies, and weak or poleward winds with cloudy skies. This affects the downward longwave and shortwave fluxes in opposite ways. In summer, weak or poleward along-shelf winds also cause relaxation from upwelling which raises T_s [_Send et al._, 1987; _Lentz_, 1987a]. The cross-shelf wind velocity, although much weaker than the along-shelf component, can affect RH, especially in winter. The lowest RHs tend to occur for off-shelf winds (negative u) while higher RHs prevail for on-shelf winds.

4. C3 Heat Flux Time Series

In this section, we first estimate the uncertainty in the computed heat flux components based on the in situ measurement uncertainties, and then present the C3 daily-averaged heat flux times series for SMILE and CODE. A discussion of uncertainty in latent heat flux follows.

Experimental Uncertainties

Here we combine the in situ measurement uncertainties (Table 3) with the heat flux formulas and basic meteorological and oceanographic time series presented above to construct estimates of the resulting uncertainties in the different heat flux components. The approach

taken is to compare the hourly heat flux component time series computed with the basic variables (the base case) with that computed using input variables biased upward and downward by the measurement uncertainties in Table 3. The means and standard deviations of the difference time series for individual measurement errors are summarized by component and experiment in Table 4. Since I_{lw} was not measured in CODE, the uncertainties in the CODE daily Q_b series were estimated by comparing the daily Q_b measured in SMILE with

Table 3. Meteorological and Oceanographic Instrumentation Used in CODE and SMILE Organized by Instrument and Variables Measured

Variable	Sensor	Manufacturer	In Situ System Accuracy	Reference	Experiment
VAWR					
Wind speed/ direction	three-cup anemometer	R. M. Young (6301)*	± 2%[†]	1	CODE
	vane	R. M. Young (6101)*	...	...	...
	magnetic compass	EG&G (VACM)	< ± 8.5°	1	...
Wind speed/ direction	three-cup anemometer	R. M. Young (6301)*	± 2%[†]	1	SMILE
	vane	Custom (WHOI)	...	...	...
	magnetic compass	EG&G (VACM)	< ± 8.5°	1,2	...
Insolation	pyranometer	Eppley Laboratory (8-48)	± 5%[‡]	3,4	CODE/SMILE
	pyranometer	Eppley Laboratory (PSP)	± 5%[‡]	3,4	SMILE
	pyranometer	Hy-Cal Engineering (8405)	± 5%[‡]	1,4	CODE 2
Longwave radiation	pyrgeometer	Eppley Laboratory (PIR)	± 5%	5	SMILE
Air pressure	Digiquartz transducer	Paroscientific (215-AS)	± 0.6 mbar	3	CODE 2
	gill pressure port	Paroscientific (215-AW)	± 0.6 mbar	3	SMILE
Relative humidity	cellulose strip, strain gauge, gill shield	Hy-Cal Engineering (HS-3552B)	± 6%	1	CODE 2
	capacitive-type sensor, gill shield	Väisälä (Humicap)	± 5%	3	SMILE
Air temperature	thermistor gill shield	YSI (Yellow Springs Instruments)	≤ ± 0.4°C (wind > 3 m/s) 1-3°C (less wind plus strong sun)	1,6	all
Water temperature	thermistor	Thermometrics	± 0.1°	1	all
NDBC 13					
Air pressure	variable capacitance transducer	NDBC general service buoy payload	± 1 mbar	7	CODE 1
Air temperature	thermistor	(see air pressure)	± 1°C	7	SMILE
SIO VMCM					
Current speed	orthogonal propellors	SIO VMCM	−5%	8	CODE 1
Direction	flux gate compass	SIO VMCM	± 5°	8	...
Water temperature	thermistor	SIO VMCM	± 0.10°C	9	...
WHOI VMCM					
Current speed	orthogonal propellors	EG&G (VMCM)	−5	8	CODE 2/SMILE
Direction	flux gate compass	EG&G (VMCM)	± 5°	8	...
Water temperature	thermistor	YSI	± 0.2°C	9	CODE 2
			± 0.1°C	2	SMILE

Table 3. (continued)

Variable	Sensor	Manufacturer	In Situ System Accuracy	Reference	Experiment
WHOI VACM					
Current speed	rotor	EG&G (VACM)	0–20% overspeeding due to surface wave conditions	8	CODE 1 (C5)
Direction	vane/magnetic compass	EG&G (VACM)	± 3°C	10	...
Water temperature	thermistor	Thermometrics or YSI	± 0.1°C	9	...
BBML					
Insolation	pyranometer	Li-Cor (LI-200SB)	± 5	11	SMILE
Stewarts Point					
Insolation	pyranometer	Eppley Laboratory (PSP)	± 4%	5	SMILE
Longwave	pyrgeometer	Eppley Laboratory (PIR)	± 5%	5	SMILE

For each variable, the estimated in situ measurement uncertainty with references for the system used in each experiment is listed. PSP denotes precision spectral pyranometer (Eppley); PIR denotes precision infrared radiometer (Eppley). References are as follows: 1, *Dean and Beardsley* [1988]; 2, *Trask et al.* [1989]; 3, *Weller et al.* [1990]; 4, *MacWhorter and Weller* [1991]; 5, R. E. Payne (personal communication, 1996); 6, *Payne* [1987]; 7, *Hamilton* [1980]; 8, *Beardsley* [1987]; 9, *Irish* [1985]; 10, *Bryden* [1976]; 11, LiCor, Inc. technical information.

* Modified at Woods Hole Oceanographic Institution (WHOI). The three-cup anemometors used in CODE (model 06020A cupwheel) and SMILE (model 12170C cupwheel) were modified at WHOI to interface with the VAWR counting circuitry.

† Does not include estimated effect of cup overspeeding.

‡ Includes estimated effect of sensor tilt (the insolation sensor was ungimballed).

that computed using (4) and (5) with different inputs (e.g., by replacing the RH measured in SMILE with its (constant) median value to mimic CODE 1). In general, the largest uncertainties are less than ±15 W m^2 and arise from the measurement uncertainty in I_{sw} and RH.

Based on Table 4, estimates of the maximum uncertainties for each component have been made using the combination of modified input variables which lead to the largest difference from the base case. These estimates are listed in Table 5 together with estimates of the maximum uncertainty in Q_n. In all experiments, the uncertainty in Q_s was smaller than for other components, and in CODE 2 and SMILE when RH was measured, the uncertainty in Q_l was largest. The decrease in uncertainty in Q_l in SMILE in comparison to CODE reflects primarily the reduced insolation during winter.

C3 Daily-Averaged Heat Fluxes

C3 daily-averaged surface heat flux time series are presented next for SMILE (Figure 6), CODE 2 (Figure 7), and CODE 1 (Figure 8), and their statistics are summarized in Table 6. Daily-averaging eliminates di-

urnal variation in Q_i, and the resulting time series better illustrate the importance of different components on timescales of days to months. Between mid-November and the end of February, the average net heating is indistinguishable from zero. Net heat fluxes from March to May and in the summer months are large and positive. In each experiment, Q_i is the largest single mean component, followed by Q_b. Q_l and Q_s are weaker and about the same magnitude. This is generally true for their fluctuations (as indicated by the similar magnitude of their standard deviations) as well as means. Both the mean Q_l and Q_s vary in sign. In winter and in spring prior to the spring transition, they almost always represent a transfer of heat from the ocean to the atmosphere. In summer, Q_s is usually from atmosphere to ocean due to coastal upwelling, and the Q_l varies in sign depending on RH.

The linkage between different heat flux components is demonstrated in Figure 9. The connection is clearest between the net downward shortwave and net upward longwave fluxes, which are both greatest on cloudless days. Cloudless days are often associated with equatorward winds, especially in the spring and summer upwelling season (as represented by the entire CODE 2
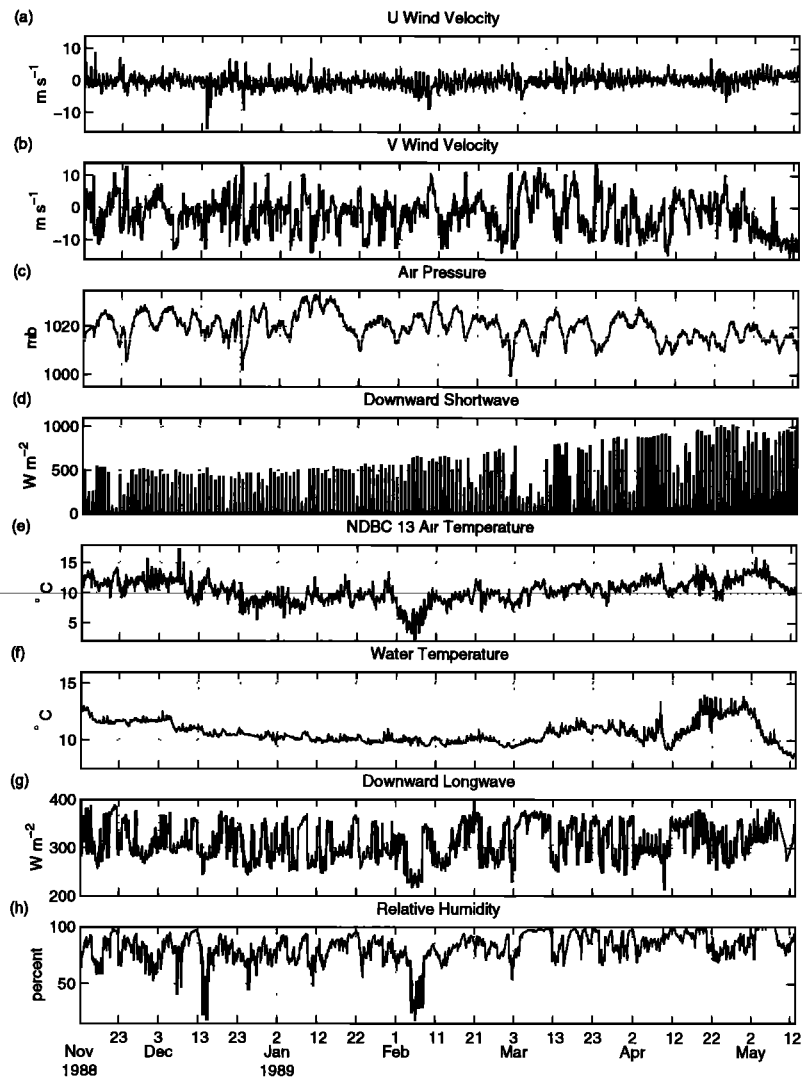
Figure 3. Hourly-averaged meteorological time series from SMILE: (a) on-shelf wind; (b) along-shelf wind (with positive v poleward); (c) air pressure; (d) insolation; (e) air temperature; (f) water temperature; (g) downward longwave radiation; and (h) relative humidity. SMILE spans winter and spring and includes the spring transition which starts May 1, 1989. To facilitate comparison between Figures 3, 4, and 5, these time series are plotted with common horizontal and vertical axes lengths.

period), but also to some extent in winter (SMILE, November through February). Between November and February, Q_i and Q_b means and variability are similar in magnitude and tend to cancel, so that variation in Q_i and Q_b has relatively little effect on net heat flux variability during this time. Beginning in spring, Q_i means and daily-averaged fluctuations become much larger, since the effect of clouds on reducing I_{sw} is proportional to I_{sw}, which increases significantly from winter to summer. This allows Q_i to drive both the mean net heat flux and much of its variability in summer. In winter, the relative balance between Q_i and Q_b allows Q_l and Q_s, which are generally negative and correlated to each other during this period, to become important to the mean Q_n and

its variation. In summer, variability in the combined Q_l and Q_s remains similar in magnitude to that in winter and continues to be important to net heat flux variability.

Uncertainties in Positive Latent Heat Flux

The C3 heat flux series presented above show large latent heat fluxes into the ocean of order 50 W m^{-2} or more during the 1989 spring transition (Figure 6) and summer 1982 upwelling season (Figure 7). Associated with advection of very moist, warm marine air over cool upwelled water on the shelf, the resulting positive air-sea specific humidity difference leads (we think) to direct condensation on the sea surface, thus causing positive Q_l. The magnitudes of these large positive
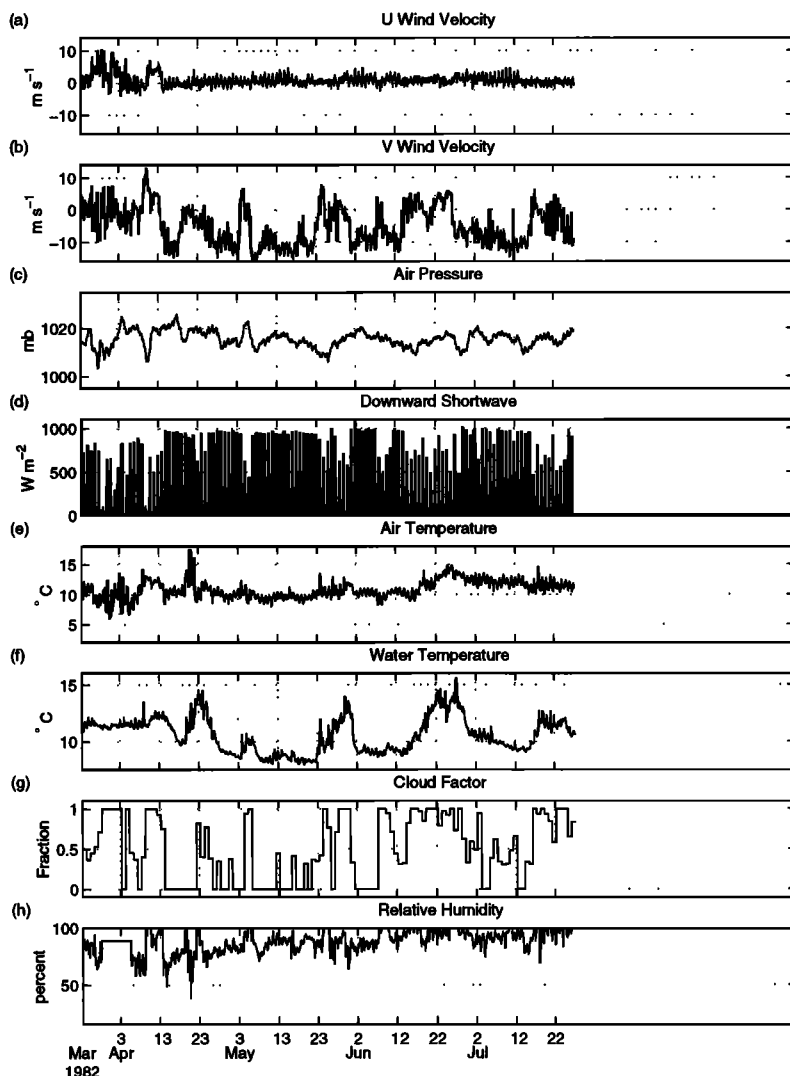
Figure 4. Hourly-averaged meteorological time series from CODE 2. Panels correspond to those in Figure 3, except for Figure 4g which shows the daily-averaged cloud factor. CODE 2 includes the 1982 spring transition which began in April 14.

latent fluxes must be interpreted with caution for several reasons. Positive Q_l values depend strongly on the accuracies of both RH measurements near 100% and the surface skin temperature. The RH sensors used in CODE and SMILE were routinely calibrated up to values of about 94%, and values above 94% may have uncertainties larger than those reported in Table 3 (Appendix A). If the RH measurements are taken as correct, the magnitude of the positive latent flux is not particular to the TOGA/COARE formulation (since both TOGA/COARE and LP codes yield similar magnitudes). The difference between the true skin temperature and our bulk measurement T_s at an effective depth at ~ 0.5 m (Appendix A) is difficult to estimate, but we have assumed that the difference is insignificant since the wind was generally strong when insolation was large (i.e., during the upwelling season).

Of more concern is the applicability of the bulk estimates to the set of conditions found in this shelf region.

These formulae were developed for quasi-steady open ocean conditions with negligible spatial gradients in air and ocean surface fields. As air flows over the northern California shelf, it must adjust to the coastal orography and changes in surface conditions such as aerodynamic roughness and temperature. During the upwelling season, the flow of warm marine air over cool upwelled water leads to a stable marine layer and development of internal boundary layers associated with strong T_s changes. Scaling arguments summarized by *Fairall and Markson* [1987] and *Garratt* [1990] suggest that our atmospheric measurements were made sufficiently close to the ocean surface (≤ 3.5 m) to be within a quasi-equilibrium layer where bulk formulations should provide good estimates of the turbulent air–sea fluxes during both unstable and stable conditions.

While the stable case of warm air flowing offshore over cool water has been examined experimentally [*Garratt and Ryan*, 1989] and numerically [*Garratt*, 1987], much
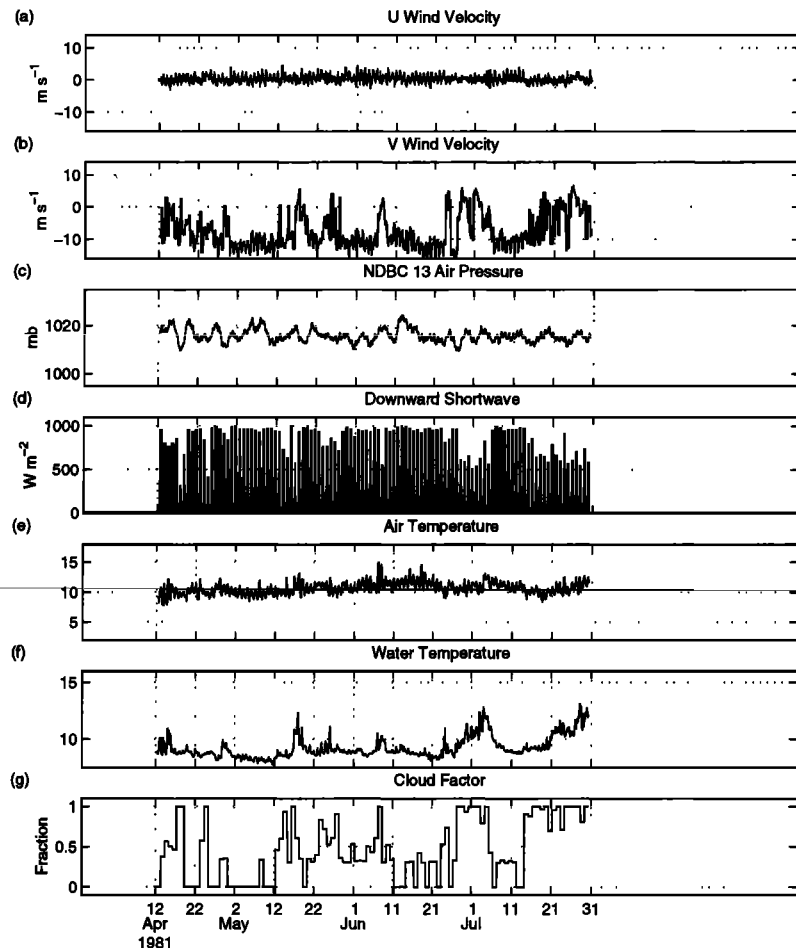
Figure 5. Hourly-averaged meteorological time series from CODE 1. CODE 1 begins after the 1981 spring transition.

less is known about the case of warm, moist airflow over cold water well away from land. We can find only one published report [*Anderson and Smith*, 1981] of direct eddy flux measurements of downward vapor flux over water corresponding to $Q_l \approx 20$ W m^{-2} made during stable atmospheric boundary layer conditions on the outer Scotian shelf. For comparison, for high dew-fall over land, Q_l can reach 50 W m^{-2} for 10-m wind speeds less than 6 m s^{-1} [*Garratt and Segal*, 1988]. For lack of additional information, we will present Q_l as computed using (7) but note that the magnitudes of the large positive latent fluxes may be overestimated during extreme condensation conditions.

5. Surface Heat Flux Events in Different Seasons

Atmospheric forcing and the surface heat flux also exhibit significant variability on timescales of hours, especially during synoptic weather events. To gain insight into this variability, we present next hourly time series during several characteristic events in winter, spring, and summer.

Winter Events

Winds over the northern California shelf during winter are characterized by strong poleward and equatorward fluctuations with timescales of several days (Figure 3) [*Dever and Lentz*, 1994; *Dorman et al.*, 1995]. These fluctuations tend to be stronger in the along-shelf direction due to the coastal mountain range (Figure 1) and are caused by the passage of both low (cyclonic) and high (anti-cyclonic) pressure systems over the coast from the northwest. These wind events are typically separated by periods of weaker and more variable winds.

Figure 10 illustrates a period of initially weak and variable winds followed by poleward and equatorward winds. The synoptic weather pattern for this period is shown in Figure 11. By February 4, a large-scale low had developed over the U.S. southwest while a high formed over the U.S. central northwest. This cyclone-anticyclone pair carried very cold, dry continental air westward and southward over northern California. This synoptic pattern persisted for several days until a new low crossed the southern California coast on February 9, bringing warm, moist marine air over the northern California shelf.

Table 4. Sensitivity of Heat Flux Components to Individual Measurement Uncertainty in the Different Field Experiments

		CODE 1 Sensitivity to Individual Measurement Errors					
		$T_a \pm 0.4°$	$T_s \pm 0.1°$	$RH \pm 5\%$	$I_{sw} \pm 5\%$	$I_{lw} \pm E$	$U - 6\%$
Q_i	mean	...	...	...	±13	...	...
	s.d.	...	...	...	±17	...	...
Q_{best}	mean	±2	0	...	±7	...	...
	s.d.	±1	0	...	±8	...	...
Q_l	mean	±6	±2	...	...	...	0
	s.d.	±3	±1	...	...	...	±1
Q_s	mean	±5	±1	...	...	...	−1
	s.d.	±2	±1	...	...	...	±1
		CODE 2 Sensitivity to Individual Measurement Errors					
		$T_a \pm 0.4°$	$T_s \pm 0.1°$	$RH \pm 5\%$	$I_{sw} \pm 5\%$	$I_{lw} \pm E$	$U - 6\%$
Q_i	mean	...	...	...	±12	...	...
	s.d.	...	...	...	±16	...	...
Q_{best}	mean	±2	±1	± 1	±6	...	...
	s.d.	0	0	± 1	±8	...	...
Q_l	mean	±7	±3	±13	...	...	2
	s.d.	±5	±4	± 7	...	...	±3
Q_s	Mean	±4	±1	0	...	...	0
	Std	±2	±1	0	...	...	±1
		SMILE Sensitivity to Individual Measurement Errors					
		$T_a \pm 0.4°$	$T_s \pm 0.1°$	$RH \pm 5\%$	$I_{sw} \pm 5\%$	$I_{lw} \pm E$	$U - 6\%$
Q_i	mean	...	...	...	± 7	...	...
	s.d.	...	...	...	±12	...	...
Q_b	mean	...	±1	...	0	±15	...
	s.d.	...	0	...	0	± 2	...
Q_{best}	mean	±2	±1	±1	±2	...	...
	s.d.	0	0	±1	±4	...	...
Q_l	mean	±5	±2	±9	...	...	2
	s.d.	±3	±2	±5	...	...	±2
Q_s	mean	±3	±1	0	...	...	0
	s.d.	±2	0	0	...	...	±1

The mean and standard deviation are between hourly heat flux components calculated with the C3 basic data and those biased by the uncertainty in each variable. Units are W m^{-2} and are rounded to nearest integer. The uncertainty in downward longwave measurements E are $\pm$ 10 W m^{-2} in day and $\pm$ 5 W m^{-2} at night.

Despite initially weak winds (often less than 5 m s^{-1}) and clear skies, the daily-averaged Q_n losses on February 6 and 7 are among the largest observed during SMILE. This occurs because the Q_b loss nearly cancels out the Q_i gain and the very cold, dry continental air flowing over the shelf boosts both Q_l and Q_s losses. On these days, diurnal cycling is most evident in T_a and RH (due in part to nighttime cooling over land) rather than in the wind. It affects hourly Q_s and Q_l fluxes with maximum losses occurring in (local) early morning hours. Although the daily-averaged fluxes are large in magnitude in comparison to other SMILE days, they remain dwarfed by the diurnal variation in Q_i.

Weak winds continue on February 8 accompanied by increasing RH, T_a, and cloudiness as the offshore low approaches from the southwest. In response to this, the magnitudes of all heat flux components decrease. On February 9, the wind becomes poleward and stronger, causing only a small increase in Q_s and Q_l as the air–sea temperature difference decreases and specific humidity rises. Diurnal variability in Q_l and Q_s fluxes is not evident on these days. As poleward winds weaken on February 10 and 11, Q_n becomes positive. The weak Q_n fluxes between February 9 and 11 are close to the average for SMILE between November and the end of February.

Table 5. Sensitivity of Heat Flux Components to the Combined Maximum Measurement Uncertainties in the Different Field Experiments

		CODE 1	CODE 2	SMILE
Q_i	mean	±13	±12	± 7
	s.d.	±17	±16	±12
Q_b	mean	± 9	±10	±16
	s.d.	± 8	± 8	± 2
Q_l	mean	± 8*	±20	±15
	s.d.	± 4	±11	± 9
Q_s	mean	± 6	± 5	± 4
	s.d.	± 3	± 3	± 3
Q_n	mean	±35	±47	±42
	s.d.	±20	±22	±15

Listed are the means and standard deviations of the difference time series computed using C3 basic hourly data and the C3 data biased by the combination of measurement uncertainties which gives the maximum positive negative) heat flux biases. The uncertainties in Q_n were computed assuming the uncertainties in the four heat flux components are independent. Units are W m^{-2}.

*The uncertainties given for Q_l in CODE-1 (where RH was not measured) reflect the uncertainty in other input variables. Actual Q_l uncertainty in CODE 1 is unknown, but probably comparable to or larger than that observed in CODE 2.

On February 12, the wind becomes equatorward and is accompanied by clear skies and a slightly lower RH. Again, changes in Q_i and Q_b net compensate. The Q_l loss increases to near 100 W m^{-2} due to the reduced RH, while the Q_s loss remains fairly low (around 20 W m^{-2}). The daily-averaged Q_n is negative and fairly weak during this time (between 20 and 40 W m^{-2}). Diurnal variability in Q_l is again present, but during this period it is forced by diurnal wind variability rather than T_a or RH (which remain fairly constant). Maximum Q_l losses on February 12–13 (and to a lesser extent on February 14) occur during local afternoon and evening hours when wind speed peaks.

Figure 10 demonstrates several characteristics of the surface heat flux variability in winter. As mentioned above, daily-averaged net Q_i and Q_b fluxes tend to cancel each other (Figure 9). This allows variability in other meteorological variables to have an appreciable affect on the net flux, so that heat fluxes of similar magnitude can occur for quite different conditions (see Figures 3, 6, and 10). For example, the largest heat loss in Figure 10 occurs on February 6 during clear skies with weak wind (about 3 m s^{-1}) accompanied by very low T_a (about 4°C) and RH (about 35%). Similar heat losses occur on December 25 during clear skies with strong winds (about 8 m s^{-1}), and on December 24 during cloudy skies with weaker winds (about 4 m s^{-1}). Dur-

ing this 2-day period, moderately low T_a (about 8°C) and RH (70–76%) combine to produce large Q_l and Q_s losses (about 140 W m^{-2}) which approximately equal the net surface heat loss on these two days.

In winter, the correlation of Q_s and Q_l together with the compensation between Q_i and Q_b causes Q_n to be controlled largely by the air–sea (Q_l plus Q_s) heat flux. During this time, low T_a is associated with low RH resulting from the offshore advection of cool, dry continental air by high- and low-pressure systems as they move eastward across the coast.

Although atmospheric forcing continues to be driven by storms until the spring transition, the relative balance between different heat flux components changes in March when strengthening insolation causes a persistently positive daily-averaged Q_n and becomes a dominant part of its variability.

Spring Transition

The atmospheric spring transition marks the end of the winter storm season and onset of the spring/summer coastal upwelling season. During this transition, the Aleutian low weakens and splits into weaker lows over Asia and the Aleutian Islands, the North Pacific subtropical high strengthens quickly and spreads northward and eastward toward California, and a persistent low pressure cell develops over the southern United States and Mexico [Lentz, 1987b; Strub and James, 1988]. Over the U.S. west coast shelf north of Point Conception, strong and persistent equatorward winds develop in several days which initiate coastal upwelling [Strub et al., 1987]. This basic large-scale pattern then persists well into summer.

The timing of the spring transition varies from year to year as does its effect on the surface heat flux. Here we examine the surface heat flux during the May 1989 spring transition and contrast it with that during the April 1982 spring transition. Both spring transitions are marked by a period of strong equatorward winds lasting approximately 5 days and subsequent coastal upwelling which causes a decrease in T_s of 3°–4°C. Despite these similarities, other meteorological conditions lead to net heat fluxes which are quite different.

The 1989 spring transition begins on May 1, slightly later than the climatological average [Dorman and Winant, 1995] and follows the presence of a warm lens of offshore water on the shelf [Largier et al., 1993]. Although equatorward winds are generally accompanied by clear skies, clouds are often present during this spring transition (Figure 12). Despite this, insolation dominates Q_n, and its fluctuation drives much of the net flux variability. Net Q_b loss, initially near 100 W m^{-2}, declines to less than 50 W m^{-2}. This is due primarily to cloud cover and high RH and only secondarily to the decline in T_s with the onset of upwelling. Upwelling does affect Q_s and Q_l in an important way. Initially, sea and air temperatures are similar so that Q_s is weak despite
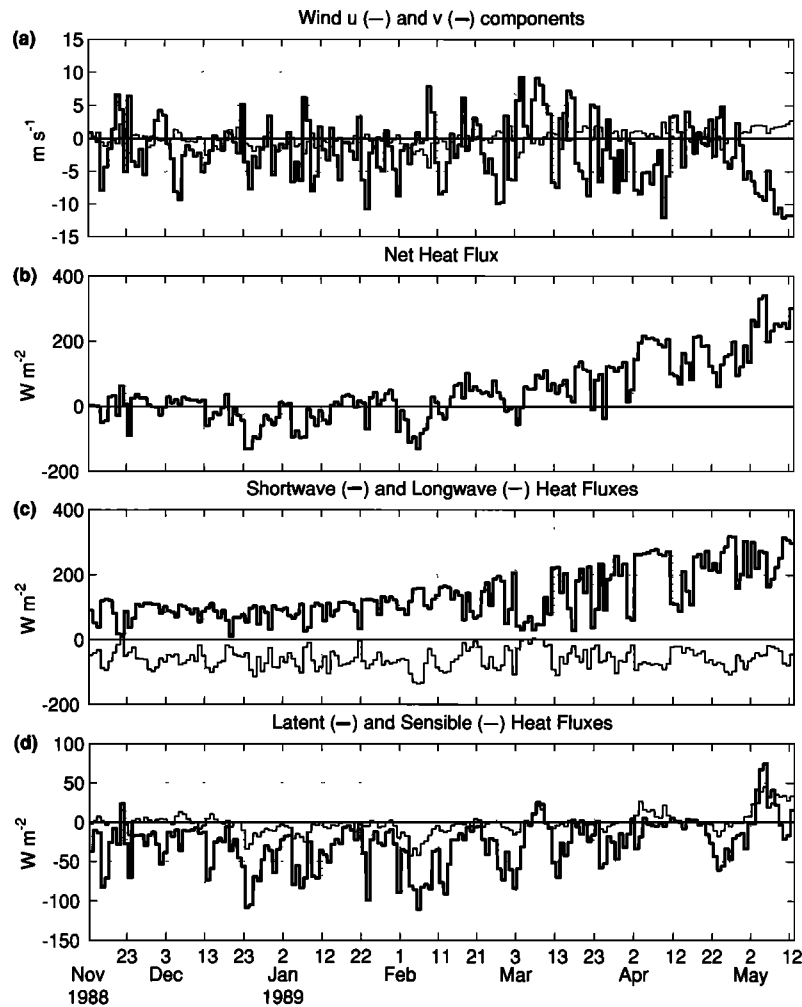
Figure 6. Daily-averaged wind velocity and heat flux time series from SMILE: (a) on-shelf (u) and along-shelf (v) wind components; (b) net heat flux; (c) shortwave and longwave fluxes; and (d) latent and sensible heat fluxes. To aid comparison between Figures 6, 7, and 8, these time series are plotted with common horizontal and vertical axes lengths and line types.

high wind speeds. Q_l loss is significant due to the specific humidity difference and high wind speed. Later, as T_s drops below T_a and the wind remains strong, Q_s becomes positive and stronger (over 50 W m^{-2} at times). The decline in T_s has a more striking effect on Q_l as estimated by (7). By May 4 through May 9, T_s is 3–4°C less than T_a. This is accompanied by RHs of near 100% and leads to a large positive Q_l associated with condensation on the sea surface. Hourly Q_l fluxes approach 100 W m^{-2} on May 5 and May 6. The addition of Q_i to these large positive Q_l and Q_s fluxes leads to the largest heat flux gains observed during SMILE. Q_l and Q_s fluxes alone nearly cancel out the Q_b loss, so that during the night, Q_n remains near zero or is even slightly positive.

As discussed in section 4.3, the large positive Q_l estimates between May 4 and May 9 must be interpreted with caution. Heat flux estimates under these conditions are sensitive to errors in T_a and RH. If RH measurements were biased high by 5% during this time, the actual positive Q_l fluxes would be reduced by 15 W

m^{-2}. The use of NDBC13 T_a in the absence of C3 T_a measurements also complicates matters. A comparison of the NDBC13 T_a with that at NDBC14 during this period shows differences ranging from $-1°$ to $+2°C$, with sign changes on timescales of 0.5 day or less. Overall, the NDBC14 T_a is slightly lower. Use of the NDBC14 rather than NDBC13 T_a does reduce latent heat fluxes, especially on May 6, but they remain positive and range up to 70 W m^{-2}. Sensor height differences between NDBC13 and C3 are expected to cause less of a problem as the TOGA/COARE code allows for different sensor heights (Table 2).

The 1982 spring transition begins on April 14 after a short period of weak winds and clouds, similar air and water temperatures, and high RH as marine air flows over the shelf (Figure 13). As the equatorward wind increases, the sky clears and the T_a and RH drop significantly as cooler, drier continental air flows offshore into the marine layer. On April 15, daily-averaged Q_n is near zero (about 9 W m^{-2}), due to the large Q_l and Q_s losses which offset the increased net radiation gain.
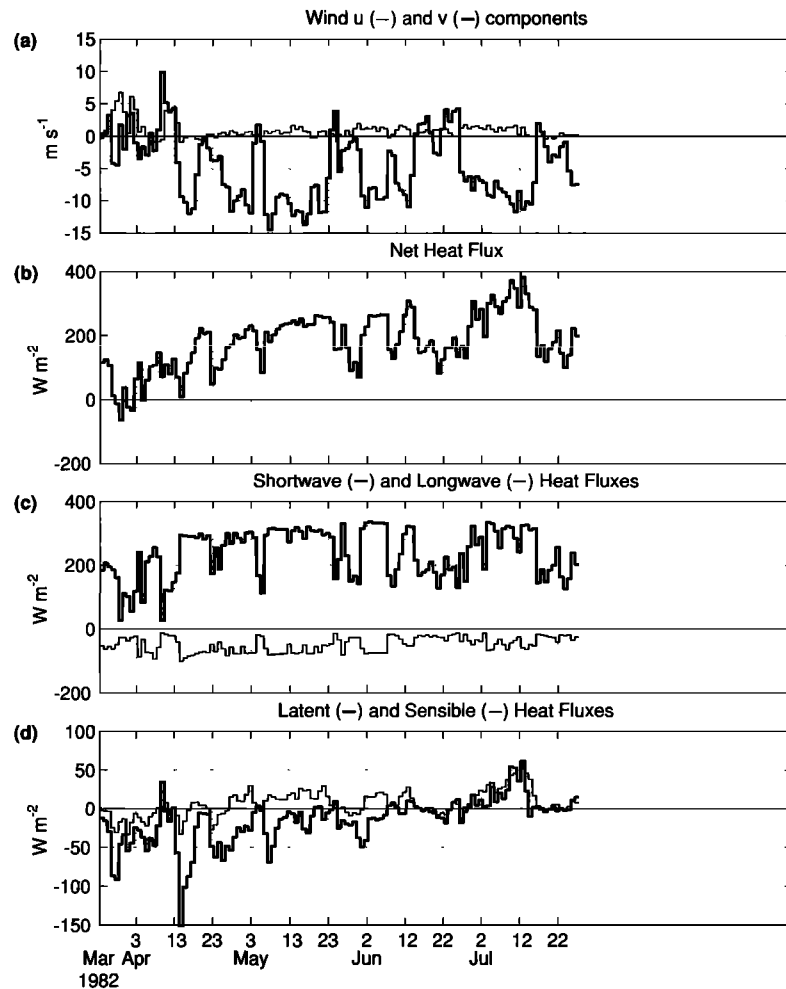
Figure 7. Daily-averaged wind velocity and heat flux time series from CODE 2.

As the spring transition progresses, Q_n becomes positive and increases over the next 5 days as RH increases and T_s drops to match T_a, both causing the Q_l and Q_s loss to decrease.

The biggest difference between the 1982 and 1989 spring transitions occurs in Q_l. It is persistently negative and much larger in 1982 while positive and weaker in 1989. This is due to the lower RHs, higher wind speeds, and negative air–sea temperature differences in 1982. The larger-scale synoptic conditions caused the 1982 spring transition to advect initially cool, dry continental air along the shelf, while relatively warm, moist marine air was carried over the shelf during the 1989 spring transition. Local wind directions during the 1982 spring transition were nearly parallel to the coast (within 5°) with a slight offshore component on most days between April 14 and 19, while the local wind direction during May 1 – 6, 1989 had an onshore component (9°–16° onshore of alongshore) (Figure 12).

Summer Upwelling and Relaxation Events

Summer winds over the northern California shelf exhibit periods of strong equatorward (upwelling-favor-

able) winds which last up to 3 weeks, separated by shorter periods of weak or poleward winds [*Beardsley et al.*, 1987]. The marine layer in summer is capped by a strong temperature inversion due to subsidence in the North Pacific high. Over the shelf, this inversion is typically located at a 30 to 200-m height, well below the top of the coastal mountain range. This situation, plus the larger-scale synoptic pattern, coastline curvature, and the coastal orography, leads to a low-level jet and supercritical flow in the marine layer over the shelf, causing winds to typically exceed 10 m s^{-1} during equatorward wind periods [*Zemba and Friehe*, 1987; *Winant et al.*, 1988; *Samelson*, 1992]. These extended periods of equatorward winds are generally cloud-free.

Shorter periods of weak or poleward winds are typically associated with cloudy skies and an increase of T_s on the shelf due to a northward flow of warm surface water from south of Point Reyes, and are termed "relaxation" events [*Lentz*, 1987a; *Send et al.*, 1987; *Rudnick and Davis*, 1988]. Several mechanisms lead to these wind relaxations and reversals, most notably the northward propagation of Kelvin waves and gravity currents in the marine layer along the central California coast
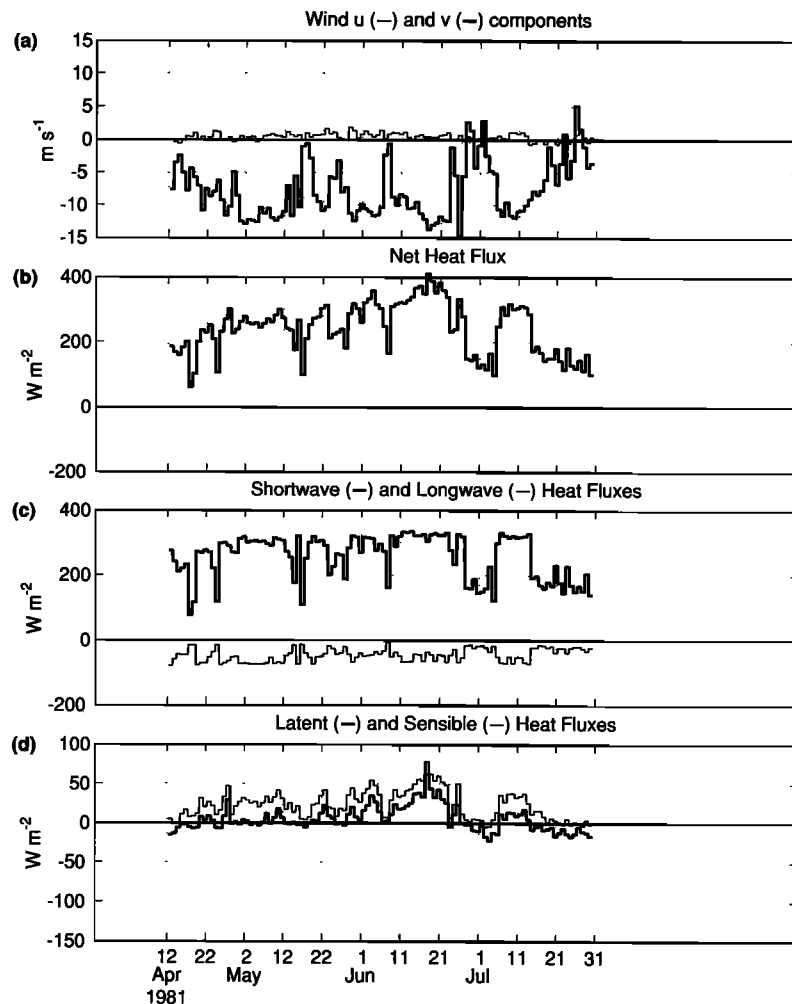
Figure 8. Daily-averaged wind velocity and heat flux time series from CODE 1.

[*Beardsley et al.*, 1987; *Dorman*, 1985, 1987]. Both processes cause the inversion to lift over the shelf from south to north, resulting in the formation of a cloud band which progresses northward.

We examine here the surface heat flux between July 12 and 21, 1982. This includes an initial period of super-critical equatorward flow over the shelf and a portion of the relaxation event which immediately follows (Figure 14). Low-level aircraft flights made on July 14 and 18 contrast the coherent spatial structure of the surface wind field during upwelling-favorable wind conditions with the lack of structure during relaxation events *Winant et al.*, 1988, see Figures 5 and 9]. The relaxation event which starts on July 13–14 in the Southern California Bight reaches the northern California shelf by July 18, and is described by *Dorman* [1987] as a gravity current in the marine layer.

Strong upwelling-favorable winds near 10 m s^{-1} occur from July 12 to July 16. These winds are accompanied by generally clear skies and high specific humidity difference as warm moist marine air flows over cold shelf water. T_a is about 1°–3°C above T_s and typically peaks

in the midafternoon. Daily-averaged Q_n during this period is strong and positive (between 280 and 380 W m^{-2}). As in the 1989 spring transition, the high air–sea temperature difference and RH cause both Q_l and Q_s gains as estimated by (6) and (7). These terms roughly balance the net Q_b loss so that Q_n flux is near zero and sometimes positive at night and quite large during the day (hourly values approach 1000 W m^{-2} at local noon).

The large shortwave and longwave fluxes found during this upwelling period are fairly typical of summer (which is dominated by active upwelling), as is positive downward Q_s. The positive downward W_l shown in Figure 14 between July 12 and July 14 is less common. It is part of a period beginning July 10 which represents the lengthiest and strongest occurrence of positive Q_l in summer 1982 (Figure 7). Earlier upwelling events are accompanied by generally lower RHs and smaller air–sea temperature differences, leading to a negative or near-zero rather than positive Q_l.

The relaxation from upwelling (as marked by the rapid decrease in equatorward winds) begins on July 18

Table 6. Statistics of the Daily-Averaged Heat Flux Time Series for Each Experiment

	Q_n	Q_i	Q_b	Q_l	Q_s
CODE 1, Summer					
Mean	241	258	−46	5	23
Maximum	411	336	−17	62	78
Minimum	61	76	−79	−22	−5
s.d.	80	68	20	15	18
CODE 2, Summer					
Mean	180	237	−49	−15	7
Maximum	382	337	−17	62	55
Minimum	−60	26	−101	−151	−33
s.d.	88	77	24	31	17
SMILE, Winter and Spring					
Mean	48	135	−59	−27	−1
Maximum	343	319	9	75	45
Minimum	−132	10	−136	−111	−43
s.d.	96	77	30	31	13
SMILE, November Through February					
Mean	−9	98	−64	−38	−5
Maximum	102	195	9	23	16
Minimum	−132	10	−136	−111	−43
s.d.	49	37	29	28	10
SMILE, March Through May					
Mean	130	189	−52	−13	6
Maximum	343	319	4	75	45
Minimum	−55	28	−109	−84	−17
s.d.	87	87	30	29	14

Units are W m^{-2}.

and continues beyond the end of Figure 14 through July 23 (Figure 4). During this period, T_s warms about 3°C to roughly match T_a and the daily mean RH remains high (> 80%), which in combination with the drop in wind speed causes Q_l and Q_s to decrease in magnitude to near zero values (less than 5 W m^{-2}). The increased cloudiness during this relaxation event reduces both the shortwave gain and longwave loss, so that Q_n is reduced to roughly 150 W m^{-2} from the July 12–16 daily mean of 300 W m^{-2}.

In summer, heat flux variability is determined by the presence or absence of upwelling-favorable winds. Clear skies accompany periods of strong equatorward winds and lead to maximum net shortwave gain. In summer, Q_i gain associated with clear skies is greater than the longwave loss (Figure 14) also associated with clear skies. Q_s fluxes are positive during equatorward winds as the air temperature is greater than the cold, upwelled water along the coast. The sign and magnitude of Q_l vary during equatorward winds. Over the summer of 1982, it is generally a loss term during May and June (Figure 7). However, in July, it can represent a gain

due to high RHs and positive air–sea temperature differences.

During relaxation events, Q_n decreases due primarily to low-level clouds and the resulting decrease in Q_i. This is to some extent mitigated by an associated increase in downward longwave radiation. This increase in downward longwave radiation is greater than the increased grey body radiative loss associated with higher T_s (Figure 14). In response to low wind speeds and reduced air–sea temperature differences, Q_l and Q_s also become quite small during relaxation events. Low wind speeds also reduce the surface mixed-layer depth to near zero [*Lentz*, 1992], effectively trapping the surface heat flux near the surface. This causes a strong diurnal cycling in T_s relative to upwelling events, despite decreased Q_n.

6. Spatial Variability in Heat Flux Components

We investigate next to what extent the C3 heat flux time series discussed above are representative of the entire shelf near C3, since short spatial differences in wind velocity, cloud cover and sea surface temperature in particular can affect the surface heat flux pattern over the shelf. Our approach is to compare daily-averaged heat flux variables measured simultaneously at two or more locations during the different field experiments. For the radiative fluxes Q_i and Q_b, we consider I_{sw} and I_{lw}. For Q_l and Q_s, we examine the effects of variability in U, T_a and T_s. Unfortunately, reliable measurements of RH exist only at C3, so that we can only speculate as to its effect on Q_l.

Insolation was measured at two or more locations during CODE and SMILE (Table 1). In Table 7a, we consider I_{sw} measured at C3 and C5 during CODE 1, at C3 and R3 during CODE 2, and at C3, Stewarts Point (SP), and the Bodega Bay Marine Laboratory (BB) during SMILE (Figure 1). Both the SP and BB records contained numerous gaps of varying length. Gaps of 2 hours or less were interpolated using a spline fit; days with longer gaps were not considered in the comparison. CODE 1 and CODE 2 comparisons encompass spring and summer months when I_{sw} is highest. SMILE I_{sw} comparisons are divided into winter and spring periods based on common coverage at the SP and BB locations. Correlation coefficients between all record pairs are highly significant, and linear regressions show a one-to-one relationship between locations to within 95% confidence limits. While it is possible coastally trapped cloud cover could lead to differences between the CODE 1 C3 and C5 average insolation, their comparison shows little evidence of this, suggesting that coastal cloud cover usually extends offshore of C5 (28 km from the coast) when present. This is in agreement with *Dorman* [1985], who presented satellite images suggesting coastally-trapped cloud cover often extends 50 km offshore of the northern California coast.
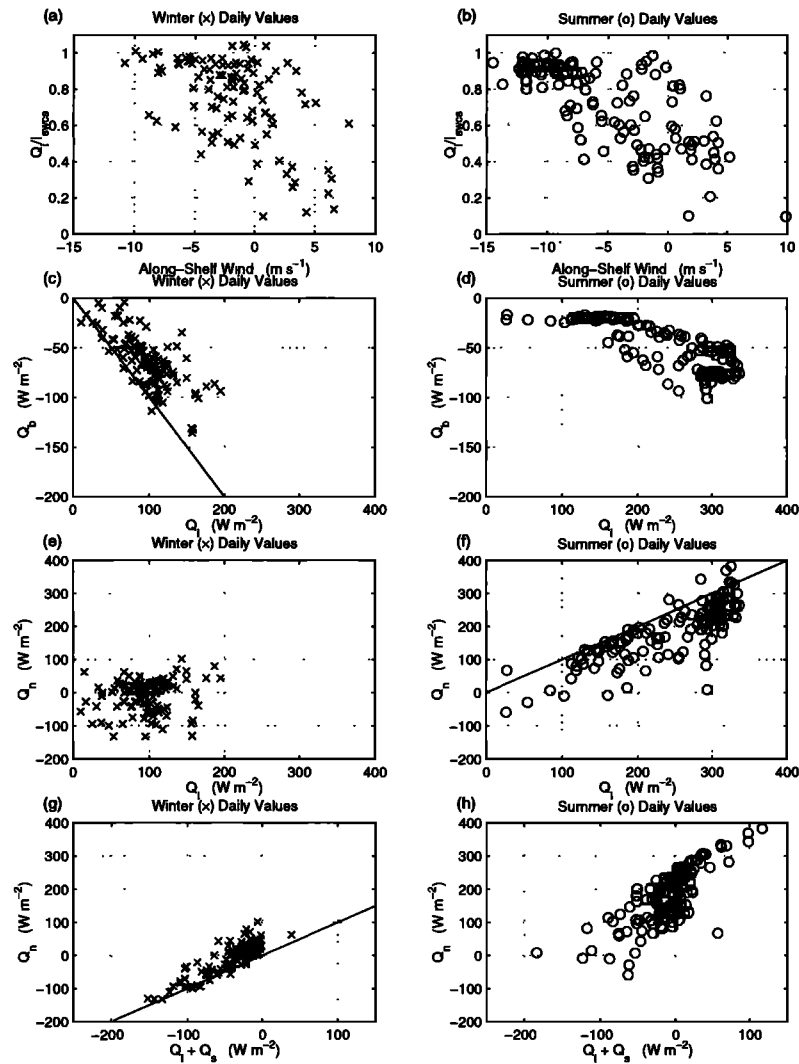
Figure 9. Relationships between daily-averaged wind speed and between various heat flux components for SMILE November 1988 through February 1989 (denoted as "winter" with crosses) on left and for CODE 2 (denoted as "summer" with circles) on right. (a,b) net shortwave flux normalized by the clear-sky value versus along-shelf wind (equatorward is negative). Values greater than 1 indicate small spatial differences in the clear-sky formula; (c,d) long-wave loss versus shortwave gain; (e,f) net heat flux versus shortwave input; (g,h) net heat flux versus air-sea flux (latent and sensible). One-to-one lines have been added to Figures 9c, 9f, and 9g to emphasize linear relationships.

Standard deviations of daily-averaged insolation differences are under 25 W m^{-2} and show no obvious dependence on cross-shelf or along-shelf direction. While isolated larger differences of up to 90 W m^{-2} occur, they have little influence on mean differences which cannot be distinguished from instrument uncertainty.

Downward longwave radiation was measured at C3 and SP during SMILE; comparison of the daily mean I_{lw} indicates little variability on scales of several kilometers (Table 7c). Even maximum differences are less than 25 W m^{-2}. Correlation coefficients are near one with regression analysis showing a one-to-one relationship within 95% confidence limits. Some weak difference may occur over the upper slope, since sea surface

temperatures are generally warmer offshore at C5. The mean temperature difference during CODE 1 is 1.4°C. This leads to a mean difference in C5 and C3 upward grey body radiation of 7 W m^{-2} during CODE 1.

U, T_a, and T_s were acquired at various sites in CODE 1, CODE 2, and SMILE (Figure 1; Table 1). These meteorological measurements were generally centered about C3 and extended 15–30 km in both directions along the 90-m isobath, and in the cross-shelf direction between C3 and the coast. In terms of their effects on surface heat fluxes, gradients in U, T_a, and T_s over the midshelf and inner shelf tend to be relatively small and short-lived. The resulting gradients in Q_l and Q_s cannot be distinguished from instrumental un-
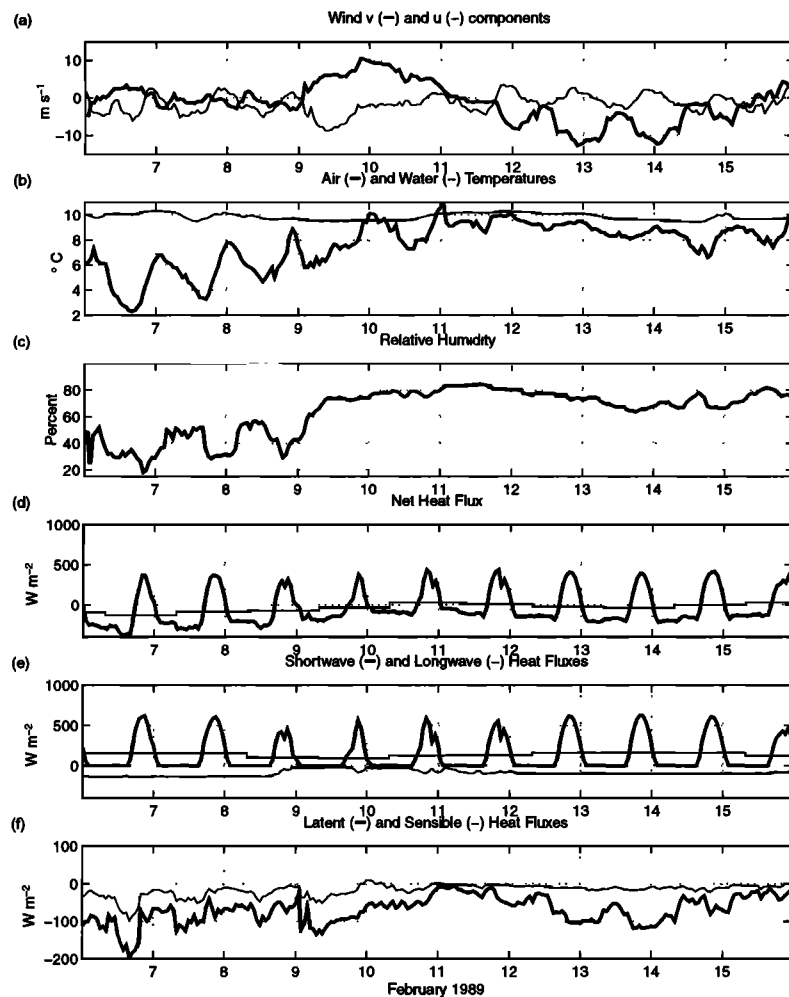
Figure 10. Hourly meteorological parameters and heat flux components during February 6–15, 1989: (a) on-shelf (u) and along-shelf (v) wind components; (b) air and water temperatures; (c) relative humidity; (d) hourly and daily averaged net heat fluxes; (e) hourly and daily averaged shortwave heat fluxes and hourly longwave flux; and (f) latent and sensible heat fluxes. Time shown in UT. To simplify comparison between this and following figures, time series are plotted with equal vertical scales, although maxima and minima are chosen to resolve variability in each time series.

certainty. However, CODE 1 did include U, T_a, and T_s measurements at C5, located over the upper slope. Between the midshelf and upper slope, differences in U, T_a, and T_s large enough to affect mean seasonal fluxes may occur. Short-scale spatial gradients in U between C3 and C5 occur for equatorward winds in winter [*Dorman et al.*, 1995] and summer [*Winant et al.*, 1988]. Also, wind-driven summer upwelling causes spatial gradients in T_s, with the coldest surface temperatures present in a coastal band and in filaments extending offshore [*Kelly*, 1985]. Both T_s and T_a are generally warmer at C5 than at C3. The combination of higher U, T_a, and T_s at C5 leads to a higher Q_l loss and smaller Q_s gain at C5 relative to C3. Assuming that the RH is constant and the same at both C3 and C5, the resulting mean net heat flux at C5 is about 30 W m^{-2} less than that at C3 (Table 6) during CODE 1.

7. Monthly Average Heat Fluxes and Comparison to Climatology

The limited spatial comparisons presented above suggest that the C3 heat flux record is representative of this shelf region in the cross-shelf direction and over at least several tens of kilometers in the along-shelf direction. This allows us to examine the monthly mean C3 heat flux values (Figure 15) and compare them to the surface heat flux climatology of *Nelson and Husby* [1983] (NH). NH estimated monthly mean surface fluxes for 1° squares in the northeast Pacific using ship report data. Here we use an average of two 1° x 1° squares (38°N, 123°W and 39°N, 124°W) which bracket C3 to obtain the NH seasonal values shown in Figure 16. We note in advance that since the NH estimates incorporate data taken over a broad area (2° in latitude, 1° in
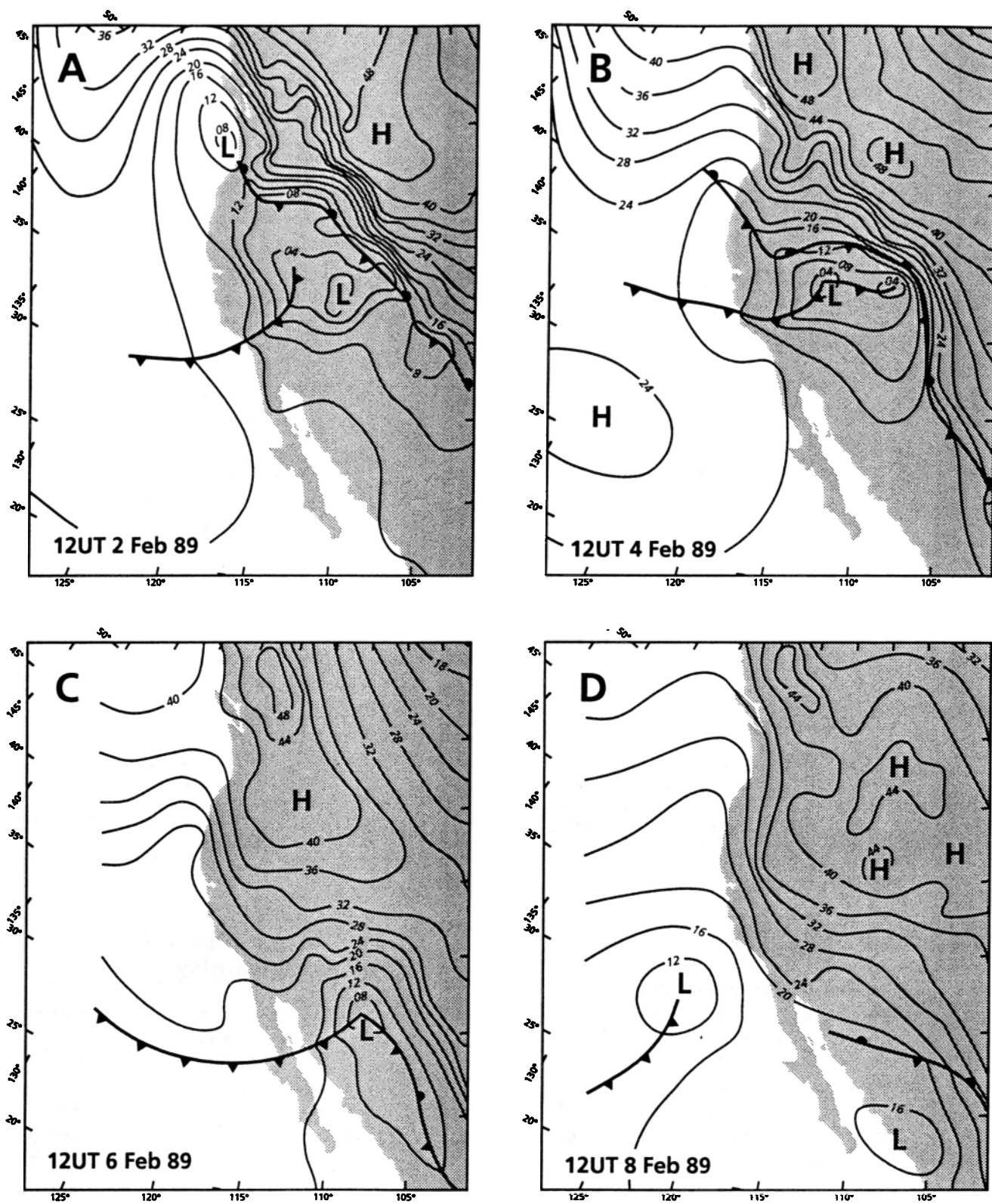
Figure 11. Surface air pressure analysis maps for 1200 UT on (a) February 2, (b) February 4, (c) February 6, and (d) February 8, 1989.
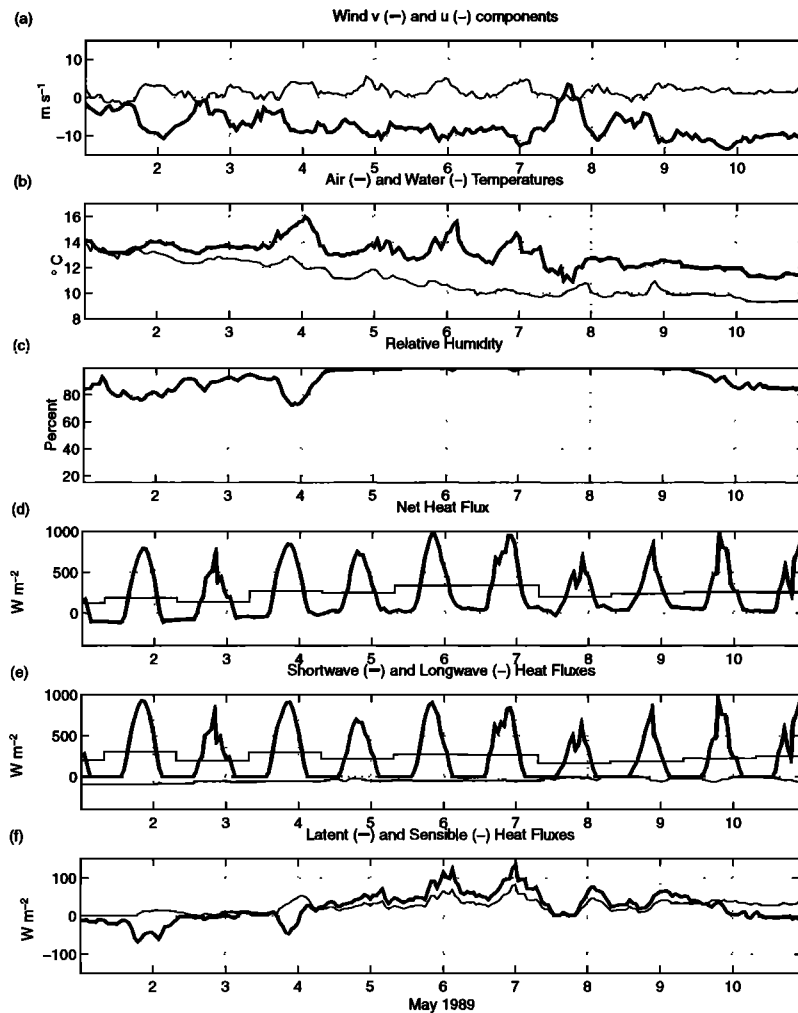
Figure 12. Hourly meteorological parameters and heat flux components during the 1989 spring transition between May 1 and 10.

longitude), they may not represent accurately the mean surface conditions and fluxes over the narrow northern California shelf.

The C3 monthly mean heat fluxes and NH exhibit similar seasonal variability. As noted by *Dever and Lentz* [1994], the seasonal cycle in Q_n is dominated by the shortwave flux, with monthly mean Q_n approaching zero in winter and 300 W m^{-2} in summer. Q_l and Q_s losses are largest in winter when the air is usually cooler than the sea surface and the lowest RHs occur. In summer, Q_s becomes positive and Q_l becomes weak and even positive during some months as the air is typically warmer than the sea surface and the highest RHs occur. While the monthly-mean Q_b indicate a larger loss in winter, it is possible this is due to interannual rather than seasonal variability. However, the general similarity in monthly net heat fluxes conceals a number of persistent differences in individual components. CODE and SMILE Q_b and Q_l, in particular, differ from NH. Estimates of longwave loss from CODE and SMILE are

greater in most months than NH would indicate, while latent losses tend to be weaker.

Differences between CODE and SMILE and NH heat flux components can arise for three basic reasons: differences in methodology, persistent spatial differences, or interannual variability. We do not believe differences in the specific formulas used to estimate air–sea heat fluxes contribute substantially to the differences noted above. The bulk formulas used by NH for latent and sensible heat fluxes contained constant transfer coefficients $C_h = C_e = 0.0013$. These are within 0.0001 of the mean TOGA/COARE transfer coefficients, and differences due to changes in these coefficients are much smaller than those which result from the large wind speed and temperature differences discussed below. The use of visually estimated cloud cover by NH is likely to cause larger uncertainties in Q_i and Q_b estimates than our radiative flux parameterizations.

To help separate spatial from interannual variability, monthly mean CODE and SMILE air–sea measure-
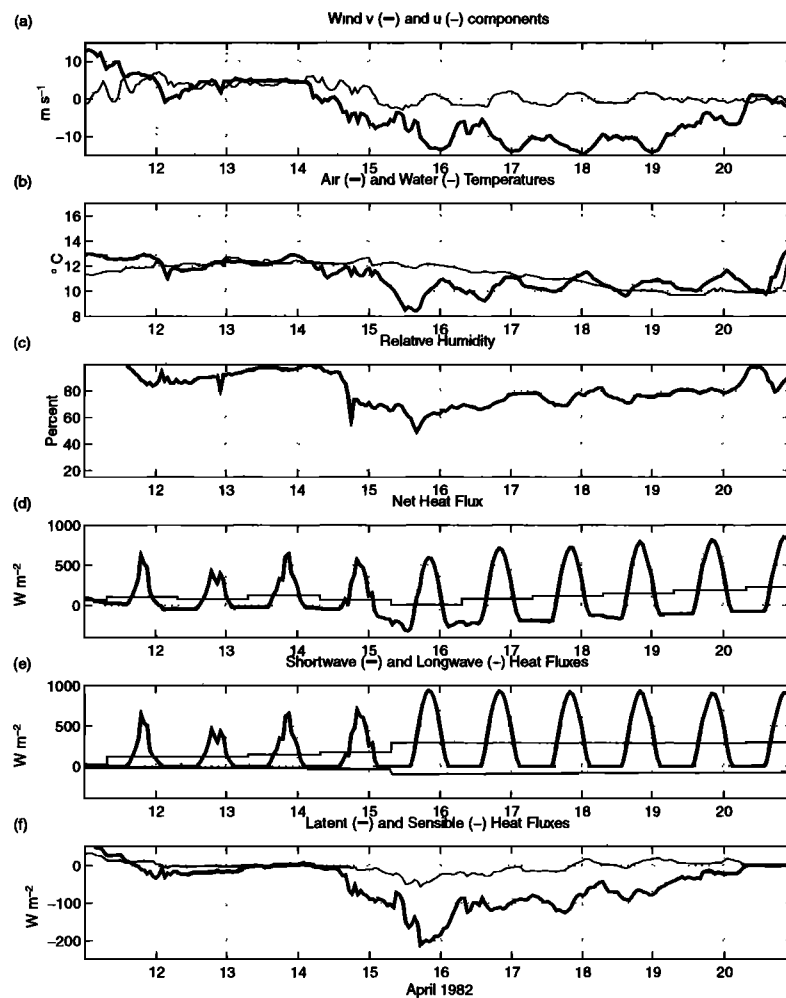
Figure 13. Hourly meteorological parameters and heat flux components during the 1982 spring transition between April 11 and 20.

ments are compared in Figure 16 with the regional NH climatology and monthly mean values of wind speed, T_a and T_s measured at NDBC13 during 1981–1990 [Dorman and Winant, 1995]. NDBC13 is located on the outer shelf about 45 km downshelf of C3 in 125-m water depth (Figure 1). While exhibiting some significant interannual variations, the CODE and SMILE C3 T_a and T_s averages tend to track NDBC13 values more closely than NH climatology, suggesting real differences between shelf and off-shelf conditions.

Short-scale variability in wind speed and direction occurs south of Point Arena during strong equatorward winds [Dorman et al., 1995; Winant et al., 1988]. Maximum summer wind speeds extend in a band south of Point Arena, while somewhat weaker speeds may exist inshore near C3 due to nonlinear behavior of the marine layer during summer [Samelson, 1992]. This short-scale wind speed variation may account for part of the differences between summer CODE wind speeds and NH climatology (Figure 16a). However, interannual variability also plays a role: the CODE 1 summer upwelling-favorable winds were unusually vigorous in comparison

with the CODE 2 summer winds, which were closer to NH values. SMILE winter wind speeds are weaker than NH values. While the C3 monthly mean winds during winter 1988–1989 were more equatorward than the 10-year NDBC13 mean, Dorman et al. [1995] report a typical number of storm-forcing events over the northern California shelf during that winter. The similarity between C3 winter 1988–1989 and NDBC13 mean wind speeds suggests that interannual variability alone cannot explain the SMILE and NH wind speed differences.

The comparisons of C3, NH, and NDBC13 T_a and T_s also indicate persistent spatial variations. With one exception (April 1982), CODE and SMILE monthly mean sea surface temperatures are lower than NH values, which resemble those found 25 km or more from the coast during CODE and SMILE hydrographic surveys [Huyer and Kosro, 1987; Limeburner and Beardsley, 1989a,b,c] and do not exhibit a minimum in spring and early summer associated with coastal upwelling (Figure 16d). CODE and SMILE monthly mean T_a values are likewise lower than the NH climatology (Figure 16c). Interannual variability is partially respon-
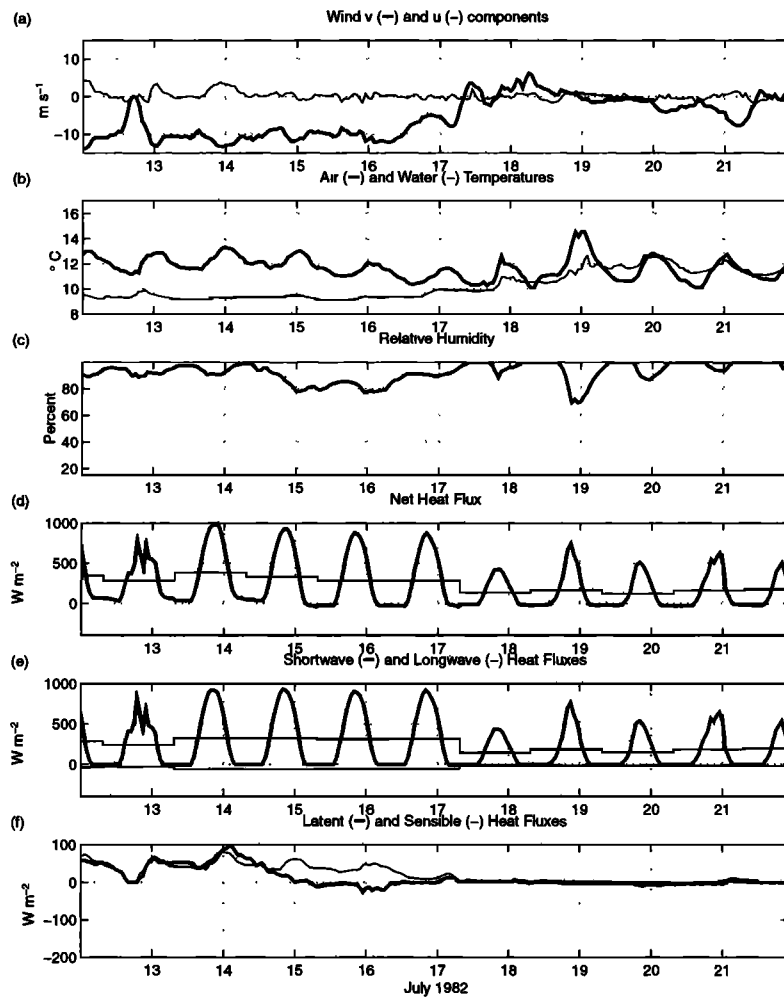
Figure 14. Hourly meteorological parameters and heat flux components during July 12–21, 1982. A relaxation event starts July 17.

sible for some differences. The C3 CODE 1 sea surface temperatures are more than 1 standard deviation less than the NDBC13 10-year mean. This is consistent with the stronger than normal upwelling-favorable winds observed that year. Likewise, the C3 SMILE winter air and sea surface temperatures are lower than the NDBC13 mean values, although air–sea temperature differences are closer to climatology.

Differences in cloud cover and RH, while occasionally large, exhibit less persistent biases. There is the suggestion that winter cloud cover and RH are lower at C3 than climatology, while the opposite situation could happen in spring and summer. However, we are unable to assess the relative importance of spatial versus interannual variability here.

8. Summary and Conclusions

Moored measurements of insolation, downward longwave radiation, wind velocity, relative humidity, air and sea surface temperature, and ocean current made in the Coastal Ocean Dynamics Experiment (CODE) and

Shelf Mixed Layer Experiment (SMILE) have been used to estimate surface heat fluxes at a midshelf site over the northern California shelf between Point Arena and Point Reyes. Taken together, the CODE and SMILE observations cover most of the seasonal cycle from winter to late summer. They include the 1982 (CODE 2) and 1989 (SMILE) spring transitions.

While imperfect, these measurements provide useful estimates of surface heat flux components. Insolation was measured in each experiment to provide estimates of the net shortwave flux Q_i. Latent and sensible heat fluxes Q_l and Q_s are estimated using the TOGA/COARE formulation [Fairall et al., 1996]. The net longwave flux Q_b is estimated directly from downward longwave radiation measurements and upward grey body radiation in SMILE. In CODE, downward radiation was not measured, and Q_b is estimated using a modification of the Berliand and Berliand [1952] formula [Fung et al., 1984]. Estimates of net heat flux Q_n are most sensitive to measurement uncertainties in insolation, RH, and longwave radiation. Based on spatial comparisons of some heat flux variables and compar-

Table 7a. Comparisons of Simultaneous Measurements of Insolation Made in CODE and SMILE

Regression Equation	Correlation Coefficient,	N, days	Mean, Difference, $W\ m^{-2}$	Difference Standard Deviation, $W\ m^{-2}$	Separation Distance, km	Season*	
Cross-Shelf							
SP $= (+\ 4.1 \pm 21.9) + (1.00 \pm 0.13)\cdot C3$	0.97	61	-4	8	7.9	winter	(SMILE)
C5 $= (-14.5 \pm 34.1) + (1.06 \pm 0.18)\cdot C3$	0.94	109	-1	25	20.5	summer	(CODE 1)
SP $= (+\ 4.9 \pm 24.1) + (1.01 \pm 0.15)\cdot C3$	0.99	28	-6	12	7.9	spring	(SMILE)
Along-Shelf							
R3 $= (-\ 4.6 \pm 24.9) + (0.97 \pm 0.14)\cdot C3$	0.96	125	$+8$	22	26.2	summer	(CODE 2)
BB $= (-14.3 \pm 68.8) + (1.21 \pm 0.63)\cdot C3$	0.83	35	-8	20	52.1	winter	(SMILE)
BB $= (+\ 5.4 \pm 46.2) + (1.08 \pm 0.31)\cdot C3$	0.97	28	-16	23	52.1	spring	(SMILE)
BB $= (-25.4 \pm 65.1) + (1.27 \pm 0.68)\cdot SP$	.83	33	-4	19	47.8	winter	(SMILE)
BB $= (+\ 0.6 \pm 37.2) + (1.06 \pm 0.28)\cdot SP$	.97	28	-28	21	47.8	spring	(SMILE)

Comparisons of simultaneous measurements of daily-averaged insolation made in CODE and SMILE are shown. Nonlinear regression formulas are given for different pairs of records based on cross-shelf or along-shelf orientation of the pairs and season. The SMILE data has been split into a winter and spring period, while both CODE 1 and CODE 2 have been taken as representative of summer. All times listed above are UT. The 95% confidence intervals are based on record lengths divided by integral time scales estimated for daily-averaged insolation for each season listed above and an equal a priori standard deviation from the nonlinear least squares fit for each of the two records considered. Integral timescales were 3 days for winter SMILE, 4 days for spring SMILE, 5 days for summer CODE 1, and 6 days for summer CODE 2. The basic statistics of the individual daily-averaged downward insolation records are listed in Table 7b.

*Winter (SMILE): 0800, December 1, 1988 to 0700 February 5, 1989; spring (SMILE): 0800, March 1, 1989 to 0700 April 21, 1989; summer (CODE 1): 0800, April 13, 1981 to 0700 July 31, 1981; summer (CODE 2): 0800, March 25, 1982 to 0700 July 28, 1982.

isons with climatology [*Nelson and Husby*, 1983; *Dorman and Winant*, 1995], the midshelf Q_n time series is considered representative of the local shelf.

Surface heat flux means and variability on timescales of months break naturally into winter, spring, and summer periods. Winter (November through February) is distinguished by near-zero means. Net short and long-wave fluxes tend to covary, with small positive Q_i and negative Q_b nearly canceling. This allows variability in Q_n to be driven by latent and sensible fluxes, which are generally negative and correlated during winter. Winter weather over the northern California shelf is driven by the passage of low- and high-pressure systems over the United States west coast; however, the SMILE ob-

Table 7b. Record Statistics for Comparison Periods Used in Table 7a

	Mean, $W\ m^{-2}$	Standard Deviation, $W\ m^{-2}$	Maximum, $W\ m^{-2}$	Minimum, $W\ m^{-2}$	Experiment
			Winter		
C3	100	31	149	11	SMILE
SP	104	31	151	11	SMILE
BB	111	35	166	43	SMILE
			Spring		
C3	146	87	281	30	SMILE
SP	150	87	288	30	SMILE
BB	153	94	301	26	SMILE
			Summer		
C3	274	72	356	80	CODE 1
C5	275	75	367	66	CODE 1
C3	252	81	355	28	CODE 2
R3	244	76	341	30	CODE 2

Table 7c. Comparisons of Simultaneous Measurements of Incident Longwave Radiation Made in SMILE

Regression Equation	Correlation Coefficient	N, days	Mean Difference, $W\ m^{-2}$	Difference Standard Deviation, $W\ m^{-2}$	Separation Distance, km	Season
$SP = (-1.2 \pm 25.6) + (0.98 \pm 0.09) \cdot C3$	0.98	58	+7	4	7.9	winter
$SP = (18.6 \pm 71.3) + (0.96 \pm 0.23) \cdot C3$	0.98	29	−5	6	7.9	spring

servations show no particular type of local or synoptic condition which predisposes large net heat flux loss (or gain) in winter. For example, large daily-averaged heat flux losses (up to 130 W m^{-2}) can occur for low RH, low air temperature, and moderate wind speed, but similar losses can occur for higher RH, higher air temperature, and higher wind speed. After February, insolation becomes stronger, and its variability is no longer compensated by Q_b. Mean Q_n becomes persistently positive, and shortwave flux variability becomes an important part of the net flux variability.

The atmospheric spring transition marks the beginning of summer meteorological and oceanographic conditions over the northern California shelf. In 1982 and 1989, it is accompanied by different surface heat flux behavior. The April 1982 spring transition was marked by clear skies and strong insolation, but also by initially strong Q_l and Q_s losses. Over several days, latent and sensible losses decrease as the shelf responds to the strong equatorward wind stress. The May 1989 spring transition was marked by somewhat cloudier skies, and latent and sensible losses are modest in comparison to 1982. In 1989, as upwelling is established, Q_l becomes positive into the ocean as strong winds are accompanied by high RH and a sea surface temperature much lower than air temperature.

Summer Q_n is always positive on a daily as well as monthly mean basis. Summer heat flux variability coincides closely with the presence of upwelling. Summer upwelling is generally accompanied by strong insolation, a smaller but still positive Q_s, and even positive Q_l on occasion. In contrast, relaxation from upwelling is often accompanied by cloudy skies, weaker insolation,

Table 7d. Record Statistics for Comparison Periods Used in Table 7c

Station	Mean, $W\ m^{-2}$	Standard Deviation, $W\ m^{-2}$	Maximum, $W\ m^{-2}$	Minimum, $W\ m^{-2}$
		Winter		
C3	305	24	359	255
SP	298	23	351	253
		Spring		
C3	325	32	369	261
SP	330	31	371	259

and very small latent and sensible fluxes. Variability in insolation dominates, and daily-averaged Q_n during upwelling is usually much higher than during relaxation.

CODE and SMILE measurements show that periods of high RH, large positive air-sea temperature difference and moderate-to-high winds occasionally occur over the northern California shelf in the upwelling season. These conditions, associated with advection of very moist, warm marine air over cool upwelled water on the shelf, lead to large positive air-sea specific humidity differences and (we think) direct condensation on the sea surface. The resulting Q_l into the ocean can be of order 50 W m^{-2} or more based on the TOGA/COARE code. The uncertainty in using the TOGA/COARE code to compute Q_l in extreme condensation conditions is very much an open question. Conditions leading to strong condensation and large Q_l gains appear to occur primarily over continental margins and not over the open ocean, so that these conditions have been poorly sampled in past field studies of turbulent surface vapor fluxes conducted over the open ocean. Our results suggest additional research is needed on the nature of turbulent vapor fluxes during stable conditions when condensation may occur over the continental shelf.

CODE and SMILE provide a detailed picture of the surface heat flux and its variability on the northern California shelf between Point Arena and Point Reyes. Similar moored measurements made on the Oregon shelf near 45°N during summer 1973 by D. Halpern and coworkers [Halpern et al., 1974; Reed and Halpern, 1974] allow estimation of the surface flux for this shelf region. Here the summer heat flux is dominated by insolation, but Q_l and Q_s losses are greater due to the relatively higher sea temperatures and lower air temperatures observed over the Oregon shelf.

Recent surface heat flux estimates made for the U.S. east coast shelf provide an interesting contrast with those for the U.S. west coast presented above. *Austin and Lentz* [1998] found Q_n variability during late summer and fall 1994 at a nearshore site off Duck, North Carolina, to be dominated by the passage of low-pressure systems with their associated cold fronts. *Mountain et al.* [1996] and *Beardsley et al.* [1996] found that the seasonal surface heat flux cycle at several sites in the Gulf of Maine is controlled by large insolation in summer and large Q_l and Q_s losses in winter. These studies support the *Mooers et al.* [1976] conceptual model of surface wind stress and heat flux patterns associated with
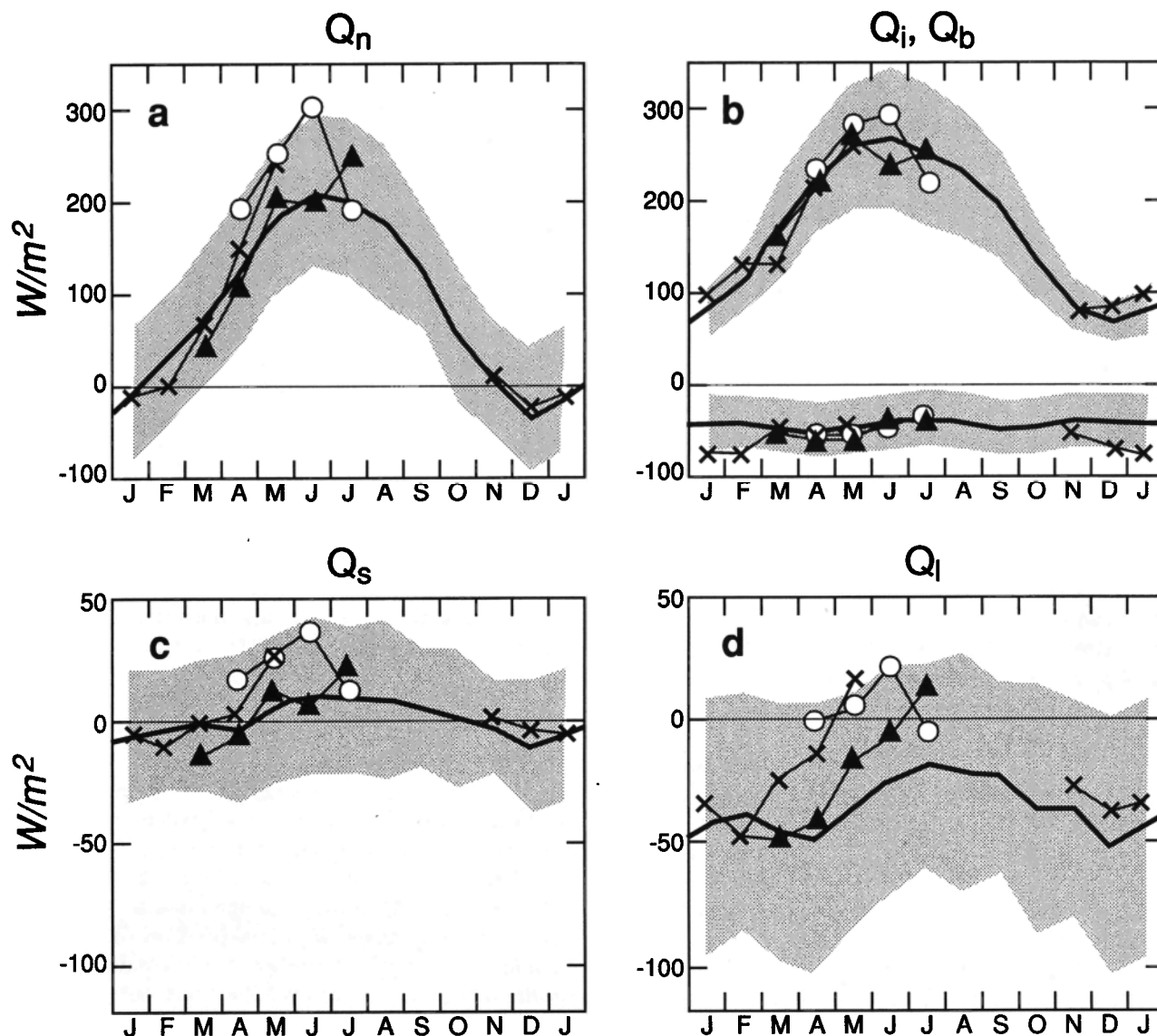
Figure 15. Monthly-averaged heat flux components: (a) net heat flux; (b) net shortwave and longwave fluxes; (c) sensible heat flux; and (d) latent heat flux. The *Nelson and Husby* [1983] annual cycles for the study area are shown as thick solid lines, with shading to indicate standard deviations of the monthly time series. Heat flux components estimated for SMILE, CODE 1, and CODE 2 are indicated by crosses, circles, and triangles, respectively.

winter cyclones which develop over the eastern United States. These storms are characterized by strong surface winds and cloudy skies, and can draw either warm moist marine air, cold dry continental air, or both, over the shelf, thus controlling the sign and magnitude of Q_s and Q_l, depending on whether the storm center tracks northeastward over the eastern United States or further east over the western North Atlantic. Maximum daily mean heat losses in winter reach about 400 W m^{-2}, while maximum heat gains in summer reach about 400 W m^{-2}. The northern California shelf also experiences maximum daily heat gains of order 350 W m^{-2} or more in summer, but maximum losses in winter only reach about 150 W m^{-2}. While the maximum heat

gains in summer are similar on both coasts (they depend primarily on insolation, a strong function of latitude), the larger heat losses in winter over the U.S. east coast reflect the large latent and sensible heat fluxes driven by winter cyclones which develop over the North American continent.

Appendix A: Measurement Problems and Their Solutions

As mentioned in section 3, not all of the meteorological and oceanographic variables needed to estimate surface heat flux were successfully measured at C3 in each experiment. We describe here in detail the methods
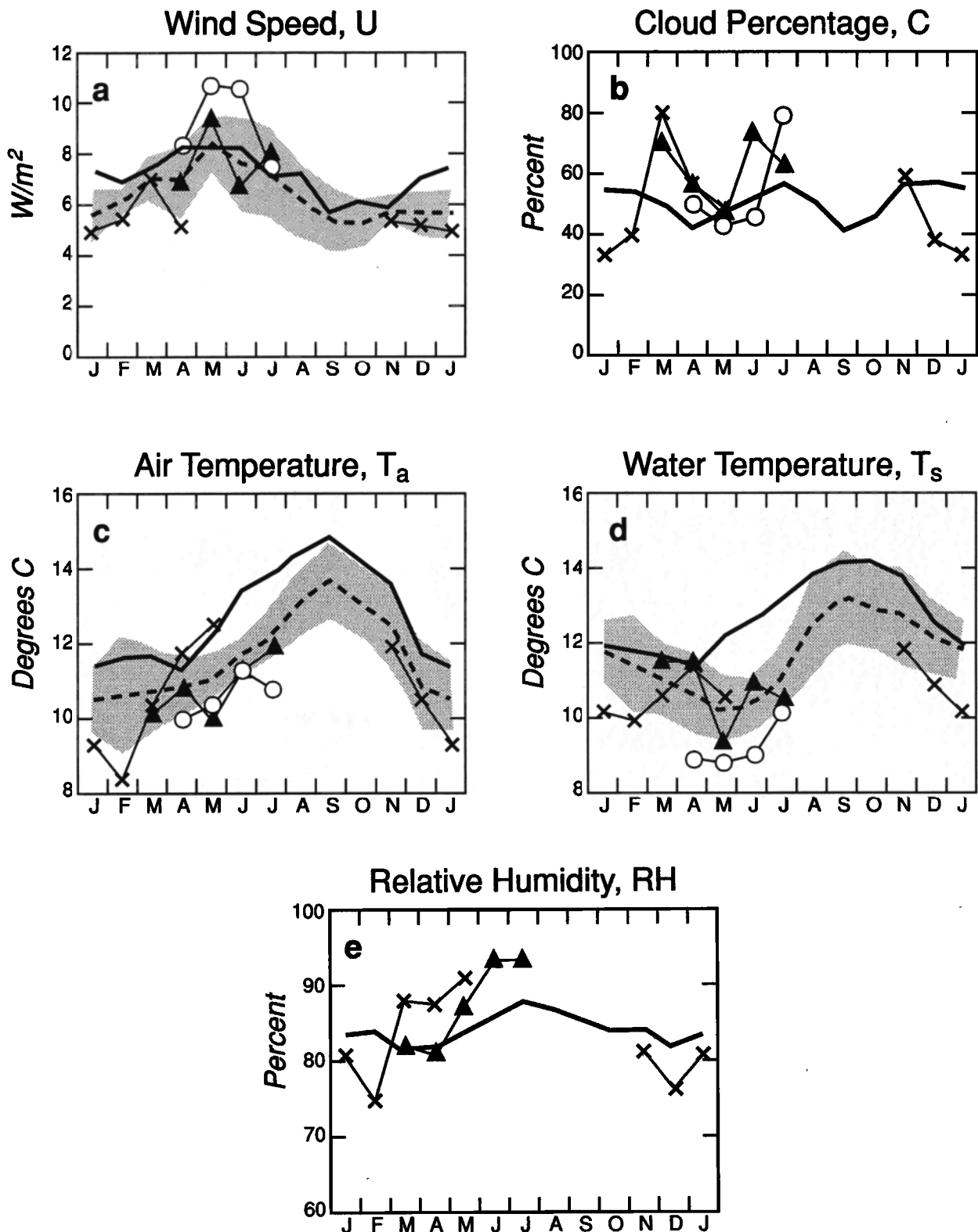
Figure 16. Monthly-averaged meteorological parameters: (a) wind speed; (b) cloud percentage; (c) air temperature; (d) water temperature; and (e) relative humidity. Meteorological parameters derived from *Nelson and Husby* [1983] (as in Figure 15) are shown by thick solid lines. Meteorological parameters measured for SMILE, CODE 1, and CODE 2, are indicated by crosses, circles, and triangles, respectively. For purposes of comparison to climatology, SMILE and CODE wind speeds, air temperatures, and relative humidities have been extrapolated to a height of 10 m using the TOGA/COARE vertical structure functions. Also shown are the 1981–1990 monthly mean wind speeds, air temperatures, and sea surface temperatures at NDBC13 (thick dashed lines) and the standard deviations of the NDBC13 monthly means (shading).

and/or assumptions used to construct the best edited time series for all variables for each experiment at C3 and for those variables at other sites used in this study.

A.1. Wind Speed and Direction

The CODE and SMILE vector-averaging wind recorders (VAWRs) returned complete wind velocity time series. Three potential sources of error in wind speed measurement are (1) overspeeding of cup anemometers due to unsteady air flow around the sensor [*Choppin*, 1982], (2) flow distortion due to the sensor location on the buoy, and (3) distortion of the mean wind profile by surface waves.

Similar Gill utility three-cup anemometers were used in both CODE and SMILE, and a comparison conducted at C3 in CODE 2 between the CODE VAWR (with separated anemometer and vane) and the prototype integral VAWR (similar in design to those used later in SMILE, see Figure 2) indicated agreement in vector-averaged wind speed to within 0.2 m s^{-1} over a speed range of 1–15 m s^{-1} and direction within 1° for wind speed >5 m s^{-1} [*Dean and Beardsley*, 1988]. While comparisons between buoy VAWR and NCAR aircraft wind data collected in CODE [*Friehe et al.*, 1984] and SMILE [*Beardsley et al.*, 1997] exhibited no evidence of significant (>5–10%) systematic overspeeding, several later comparisons between an integral VAWR and an R. M. Young model 5103 wind monitor integral propeller and vane mounted at the same height on the same discus suggest that systematic differences in wind speed between these two sensors may vary from 0% to about 6% in different experiments, with the VAWR reading high [*Trask et al.*, 1989].

The questions concerning flow distortion are difficult to address. A numerical model was used to examine the influence of the VAWR sensor supports and housing on steady potential flow past the cup area; the supports and vane caused about 0.3% increase in the model "cup speed," while the cylindrical housing contributed about 1.1% [*Norment*, 1992]. While flow distortion due to the rest of the buoy superstructure may be more important, the CODE and SMILE wind sensors were placed to minimize the influence of other sensors and the support structure, and a large steering vane was mounted on the aft end of the buoy superstructure to keep the wind velocity, air temperature, RH and air pressure sensors oriented into the wind (Figure 2).

Large et al. [1995] recently presented evidence that large surface gravity waves increase the vertical shear in the near-surface mean wind profile. This means that use of the log profile formula to compute the wind speed at 10 m from a wind speed measurement made at a lower height will underestimate the true 10-m wind speed unless corrected for wave distortion. For conditions found in CODE 1 (wind sensor height, 3.5 m; mean wind speed, 8 m s^{-1}; mean significant wave height, 2 m [*Beardsley*, 1987]), the *Large et al.* [1995] model sug-

gests that the 10-m wind speed used to compute Q_s and Q_l by means of (6) and (7) would be underestimated by 3–4%. This implies that wave distortion effects will tend to bias Q_l and Q_s low by as much as 4% on average. While no attempt was made here to correct the measured wind speed for wave distortion effects, we note that this could be easily done within the context of the TOGA/COARE or other bulk formulation provided significant wave height data are obtained as part of a moored measurement program.

In light of the uncertainty in the VAWR wind speed measurement, we have chosen to use the measured wind with no corrections for overspeeding or flow distortion in computing heat fluxes, and instead use a 6% overspeeding factor in estimating the uncertainty in the latent and sensible heat flux components summarized in section 5.

A.2. Insolation

In CODE 1, the C3 and C5 pyranometers were mounted about 0.5 m below the wind sensors, which caused partial shading on clear days with equatorward winds (about 48% of the C3 record). This shading caused a maximum error in the daily total insolation on a clear day of −2.4% at C3 and −1.5% at C5. Since the pattern of shading was quite consistent in each record, the insolation time series were corrected by removing the obvious shadows. Some consistent shading was also observed in CODE 2, and the obvious shadows were also removed. The CODE 2 C3 record had one 177-hour gap which was filled using C2 insolation data since daily-averaged C2 and C3 data generally agreed within ± 10% (although the C3 insolation was generally higher).

In SMILE, two pyranometers were mounted slightly above the other sensors and shading was not observed. However, the C3 Eppley precision spectral pyranometer (PSP) and the 8-48 data included many time gaps due in part to the partial flooding of both VAWR housings. The PSP record stopped 85 days after deployment and the 8-48 returned data until the C3 mooring was recovered. While the PSP and 8-48 series were highly correlated, the 8-48 values were consistently smaller by about 15% in comparison with the C3 PSP and a second PSP deployed at Stewarts Point (Figure 1). Since the C3 and Stewarts Point PSPs daily-averaged series were also highly correlated and differed in the mean by only 2.3 ± 8.2 W m^{-2}, the C3 PSP record was judged to be correct and the lower values of the 8-48 were attributed to scaling errors within the VAWR circuitry. Linear regression was then used to correct the amplitude of the 8-48 series, and any remaining gaps were filled using Stewarts Point PSP data. A Lycor (model LI-2005B) pyranometer mounted on the roof of the Bodega Bay (BB) Marine Laboratory (Figure 1) returned data during SMILE with some small gaps. The BB insolation time series had a nightly minimum of approximately 45 W m^{-2}, which was subtracted from the entire record to

produce the edited series used here. The moored insolation records may have some small error due to sensor tilt (none were gimballed) [*MacWhorter and Weller*, 1991], but no clear evidence was found for this in the SMILE data.

A.3. Incident Longwave Radiation

I_{lw} was not measured in CODE. In SMILE, I_{lw} was measured using two Eppley precision infrared pyrogeometers (PIR1 and PIR2) mounted on the C3 buoy and one PIR deployed at Stewarts Point. All PIRs returned useful data for much of SMILE, with some gaps, primarily in the two buoy records during the last 2 months of the experiment. The three PIR records were compared over a 124-day common period, indicating that the C3 PIR1 and PIR2 records disagreed by 4.2% on average, with PIR1>PIR2, while the C3 PIR2 record was larger than the Stewarts Point PIR by 1.0% on average. Based on the better agreement between Stewarts Point and PIR2 data, the Stewarts Point data were used to fill gaps in the PIR2 record to produce a best C3 I_{lw} series.

A.4. Relative Humidity

RH was not measured in CODE 1, so the median value observed at C3 in CODE 2 was used (89%) at both C3 and C5 at 2.7 m height. This is slightly higher than the average (85%) of the shipboard measurements made near C3 during the CODE 1 hydrographic surveys (J. Huyer, personal communication, 1985). In CODE 2, measured values of *RH* between 100 and 105% occurred frequently during periods of weak winds and reduced insolation (especially during relaxation events). The *RH* sensors used in CODE and SMILE were calibrated up to values of about 94%, and values above 94% may have uncertainties larger than those reported in Table 3 (R. Payne, personal communication, 1994). Assuming the true maximum *RH* during those periods was 100%, *RH* was corrected by clipping humidities above 100% to 100%. An alternative scheme was also tried in which humidities between 94% and 105% were linearly transformed to between 94% and 100%. Resulting latent heat flux estimates were nearly identical to the clipped *RH*s (including positive latent heat flux estimates). In the absence of any calibration information above 94%, we elected to present results for the clipped *RH*s. One 177-hour gap was filled with the record median value. In SMILE, one VAWR returned a complete good *RH* record. Isolated values above 100% were again clipped to 100%.

A.5. Air Pressure

P_a was not measured in CODE 1, so the NDBC13 time series was used at both C3 and C5. The alongshelf scale of air pressure was large in CODE 1, with the mean and standard deviation of NDBC13 minus NDBC14 hourly time series being 0.2 ± 1.4 mbar. P_a was measured at both C3 and C5 in CODE 2. The C3 record had gaps of 21 days at the beginning of the deployment and 26 days at the end. Since the mean and standard deviation of the C3 minus C5 hourly time series were -0.5 ± 0.6 mbar, the C3 gaps were mostly filled with C5 data, with the remaining gap filled with NDBC13 data.

A.6. Air Temperature

Complete T_a records were obtained at C3 and C5 in CODE 1 and at C3 in CODE 2. Unfortunately, only one SMILE VAWR was instrumented for T_a, and it returned no data. T_a was measured for the entire experiment at NDBC13 and for January 12 to May 2, 1989, at NDBC14. For the overlapping period, the mean and standard deviation of the hourly NDBC14 minus NDBC13 T_a series were $-0.2° \pm 0.8°C$, with the maximum hourly differences being about $\pm 4°C$. The decorrelation timescale of the difference series is about 1 day, so the maximum differences did not last long. The NDBC13 T_a record was used at C3, with an uncertainty in the daily-averaged T_a (as indicated by the standard deviation of its difference with NDBC14) of $\pm 0.5°C$.

A.7. Water Temperature

The CODE 1 VAWRs returned complete T_s records. In CODE 2, the C3 T_s record had one 177-hour gap, which was filled by temperature data obtained at 5 m by a vector-measuring current meter (VMCM)(corrected for bias [see *Lentz and Trowbridge*, 1991]). No VAWR T_s was obtained at C3 in SMILE. Instead, a C3 T_s series was estimated using the 6-m C3 WHOI VMCM record plus the difference between the M3 1-m VAWR and 5-m SIO VMCM temperature records. The mean adjustment was +0.10°C, while the median adjustment was under +0.03°C.

Ideally, for heat flux computations, the ocean skin temperature is desired. An experiment in the Arabian Sea (R. Trask, personal communication, 1996) recently confirmed earlier NDBC and WHOI tests showing that a 1-m temperature measurement under a 0.5-m-deep discus buoy corresponds to the temperature at about 0.5 m depth. Since the wind was generally strong when insolation was large (i.e., during summer upwelling), no additional corrections were made to the CODE and SMILE 1-m T_s records for skin temperature effects.

A.8. Surface Current

The surface currents used in the heat flux computations were taken from the shallowest VMCM at C3 and vector-averaging current meter (VACM) at C5 (see Table 3 for sensor depth). Measurements of velocity differences over the top 5 m during SMILE using a vertical array of acoustic current sensors indicate that they were generally small, less than 0.03 m s^{-1} [*Santala*, 1991].

Appendix B: Description of Surface Heat Flux Over the Oregon Shelf During July 1973

We present here surface heat flux estimates obtained from measurements made over the Oregon shelf during the Coastal Upwelling Experiment (CUE II) [*Halpern et al.*, 1974; *Reed and Halpern*, 1974]. In doing so, we have two primary motivations. The first is to enable a comparison and contrast with the summer CODE heat flux estimates obtained over the northern California shelf. The second is to present on its own merits the net surface heat flux and its components in this region. As the Oregon shelf remains an active area of modeling and observational study, we believe this is an appropriate time to revisit the CUE II data. The surface heat flux obtained from these data, though mentioned in several papers [e.g., *Bryden et al.*, 1980; *Lentz*, 1992; *Federiuk and Allen*, 1995], has yet to be presented in detail in a widely available format.

CUE II took place over the Oregon shelf in July and August 1973. For the purposes of determining the net surface heat flux, the limiting measurements are July insolation measurements [*Reed and Halpern*, 1974] at buoy B3 (location 45°15.8′N 124°7.8′W). Accordingly, we consider the heat flux there from 0800 UT, July 5, 1973 to 0700 UT, July 30, 1973. Precise system accuracy for these measurements is unknown, but many of the systems used in 1973 including the basic VAWR, Eppley model 8-48 pyranometer, and VACM were of similar design to those used in the CODE 1 experiment, and it is believed that in situ system accuracy should be similar (Table 2). The CUE II measurements also resemble the CODE 1 measurements in that no continuous measurements of RH or I_{lw} exist. For this reason, we adopt a constant RH of 85% at a height of 4 m (R. Smith, personal communication, 1996), and Q_l estimates should be viewed with caution. Also, air pressure measurements used came from the H5 mooring (107 km offshore of B3), but this is of minor concern given the small pressure effect on air–sea heat fluxes and the larger uncertainty due to RH. Other measurements used were acquired at the B3 buoy. Measurement heights for the particular instruments used are given in Table B1.

Table B1. B3 Sensor Heights Above Water During CUE II

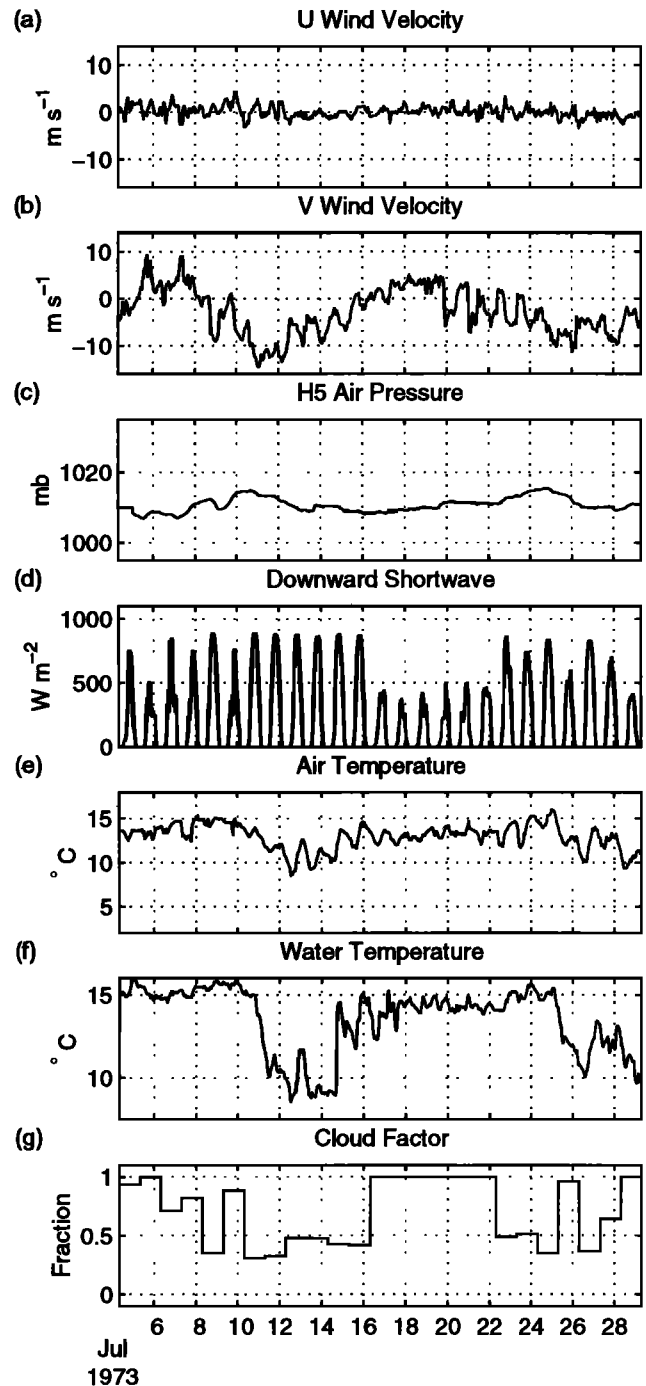| Variable	Height
Wind speed, wind direction	2.4 m
Insolation	4.0 m
Air pressure	1.8 m
Air temperature	1.6 m
Water temperature	−0.7 m
Platform	toroid

The air pressure height is that at H5.

Figure B1. Hourly-averaged meteorological time series from CUE II. Note that the daily-averaged cloud factor is always greater than 0, even on apparently clear days. See text for a discussion of the uncertainty in the cloud factor.

The hourly meteorological data and the daily-averaged cloud factor are presented in Figure B1. The CUE II data display some similarities with the summer CODE data taken some 750 km to the south. Winds are primarily equatorward, and, while statistical reliability for the relatively short 25-day record is suspect, the insolation data indicate equatorward winds are often accompanied by clear skies. One difference from the

northern California shelf is in the relative air and sea temperatures. The CUE II data indicate that even in summer, T_a is often less than T_s over the Oregon shelf. This has implications for both Q_l and Q_s. One puzzling observation is that the daily-averaged cloud factor, determined following Reed [1976], is never zero, even on several apparently clear days. This is because the observed daily-averaged insolation remains well below the clear sky insolation predicted by the Smithsonian [Seckel and Beaudry, 1973] formula used in the estimation of cloud cover. Reed [1975] first noted clear sky insolation in CUE II was only about 93% of that predicted by the Smithsonian formula but found other midlatitude insolation measurements agreed more closely with the Smithsonian formula. Measurement error on the part of the Eppley 8-48 pyranometer at B3 is unlikely to account for this discrepancy as it had been compared to calibrated instruments and found to agree to within 1% [Reed and Halpern, 1974]. Uncertainty as to the actual cloud cover is therefore a large source of uncertainty in the estimated longwave heat flux and will be discussed.

The daily-averaged heat flux components and heat flux statistics are shown in Figure B2 and Table B2. As in the CODE observations, Q_i is the largest term in the positive net heat flux. However, the mean Q_n off Oregon is substantially smaller than the July Q_n off northern California. This is due to the large Q_l loss at 45°N and to Q_s which is weakly negative off Oregon rather than positive as observed off northern California. Although the lack of RH measurements causes significant uncertainty in the CUE II and CODE 1 Q_l estimates, there is reason to believe the true Q_l loss over

Table B2. Statistics of the Daily-Averaged July Heat Fluxes off Oregon and Northern California

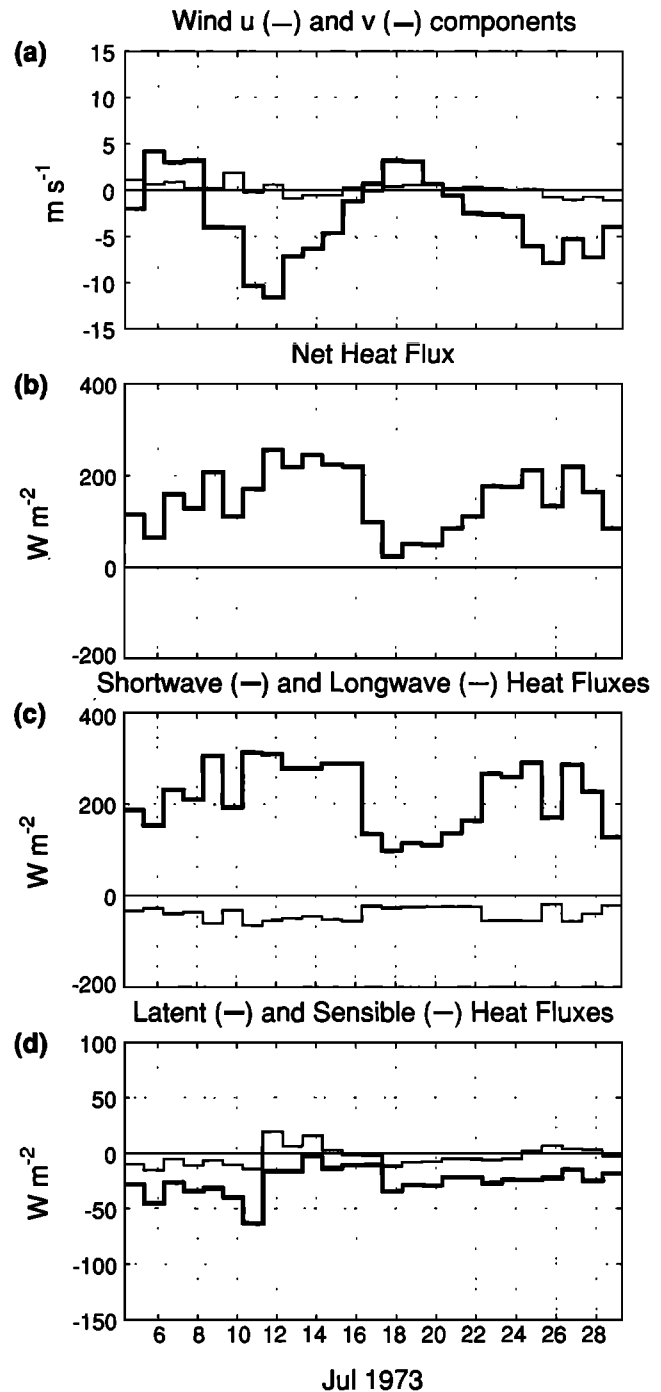|	Q_n	Q_i	Q_b	Q_l	Q_s
Oregon: CUE II B3	July 5–30, 1973				
Mean	148	216	−40	−25	−3
Maximum	256	313	−20	−3	20
Minimum	23	97	−65	−63	−16
s.d.	68	73	15	12	9
California: CODE 1 C3	July 1–30, 1981				
Mean	190	218	−35	−5	12
Maximum	319	332	−14	17	38
Minimum	99	123	−71	−22	−5
s.d.	76	73	19	11	15
California: CODE 2 C3	July 1–27, 1982				
Mean	245	249	−38	13	20
Maximum	362	334	−14	62	55
Minimum	99	126	−68	−10	−2
s.d.	62	69	17	19	18

Units are W m^{-2}.

Figure B2. Daily-averaged wind velocity and heat flux time series from CUE II. Because CUE II did not include relative humidity measurements, the latent heat flux is only an estimate based on a constant relative humidity.

the Oregon shelf in CUE II is greater than that over the northern California shelf during CODE. Over the Oregon shelf, T_a is often less than T_s. Hence, even if the RH approached 100% several meters above the sea surface, it would drop below 100% at the sea surface. In contrast, over the northern California shelf, summer T_a is often above T_s, so an RH near 100% observed several meters above the sea surface can imply an even

greater RH at the sea surface. Of course, the difference in relative T_a and T_s also affects Q_s.

Compared to Q_l and Q_s differences, mean insolation differences between CUE II and CODE are small during CODE 1 but larger during CODE 2. Although the computed mean July Q_b loss is approximately the same over the Oregon and northern California shelves, there is considerable uncertainty as to its magnitude during CUE II. The mean CUE II Q_b loss in Table B2 is based on the cloud cover estimated after *Reed* [1976] without any modifications to the Smithsonian formula. If the CUE II insolation on apparently clear days is a better measure than the Smithsonian formula of the true clear sky insolation over the Oregon shelf in July, then we have overestimated cloud cover and underestimated Q_b loss. To gauge this effect, we recalculated CUE II cloud cover based on a clear sky insolation equal to 93% of the Smithsonian formula, and used it in the estimation of the Q_b. With the lower cloud cover, the mean July 1973 Q_b loss increased by 8 W m^{-2}. The maximum increase in the daily-averaged Q_b loss was 27 W m^{-2}, and the standard deviation of the difference time series was 8 W m^{-2}.

A comparison of the 1973 CUE II mean heat flux components with the *Nelson and Husby* [1983] (NH) climatology is problematic, since the 1° x 1° square containing the B3 mooring site (centered at 45°N, 124°W) contained only 64 ship observations during July. The resulting July monthly mean values and standard errors are (in W m^{-2}) $Q_n = 209 \pm 8$; $Q_i = 243 \pm 9$; $Q_b = -35 \pm 3$; $Q_l = -10 \pm 3$; and $Q_s = 11 \pm 2$. With the exception of Q_b, the other heat flux components were smaller than climatology by 14–27 W m^{-2}, and Q_n during CUE II was about 70 W m^{-2} smaller than climatology. The primary conclusion from this is that while the NH climatology provides a useful qualitative description of the seasonal variation in the surface heat flux over the Oregon shelf, future field experiments designed to look at upper ocean processes should include surface meteorological and oceanographic measurements sufficient to allow direct estimation of the surface wind stress and heat flux (following equations 2, 3, 6, and 7). Only through direct measurement of incident shortwave and longwave radiation, wind speed, RH, T_a, and T_s can accurate estimates of surface forcing over the shelf be achieved. Fortunately, the technology to make these measurements on a moored platform with high data return has been improving and is now becoming routine. Given the importance of surface forcing on many shelf processes, we encourage making air-sea flux measurements a key component of future shelf physical oceanographic experiments.

References

Alados-Arboledas, L., J. Vida, and J. I. Jimenez, Effects of solar radiation on the performance of pyrogeometers with silicon domes, *J. Atmos. Oceanic Technol.*, 5, 666–670, 1988.

Alessi, C. A., S. J. Lentz, and R. C. Beardsley, Shelf Mixed Layer Experiment (SMILE) program description and coastal and moored array data report, *Tech. Rep. WHOI 91-39*, 211 pp., Woods Hole Oceanogr. Inst., Woods Hole, Mass., 1991.

Anderson, R. J., and S. D. Smith, Evaporation coefficient for the sea surface from eddy flux measurements, *J. Geophys. Res.*, 86, 449–456, 1981.

Austin, J. A., and S. J. Lentz, 1998, The relationship between synoptic weather systems and meteorological forcing on the North Carolina inner shelf, *J. Geophys. Res.*, in press, 1998.

Beardsley, R. C., A comparison of the vector-averaging current meter and new Edgerton, Germeshausen, and Grier, Inc., vector-measuring current meter on a surface mooring in Coastal Ocean Dynamics Experiment 1, *J. Geophys. Res.*, 92, 1845–1859, 1987.

Beardsley, R. C., and S. J. Lentz, The Coastal Ocean Dynamics Experiment (CODE) collection: An introduction, *J. Geophys. Res.*, 92, 1455–1463, 1987.

Beardsley, R. C., C. E. Dorman, C. A. Friehe, L. K. Rosenfeld, and C. D. Winant, Local atmospheric forcing during the Coastal Ocean Dynamics Experiment, 1, A description of the marine boundary layer and atmospheric conditions over a northern California upwelling region, *J. Geophys. Res.*, 92, 1467–1488, 1987.

Beardsley, R. C., S. J. Lentz, R. A. Weller, J. D. Irish, K. H. Brink, R. Limeburner, and J. D. Manning, A preliminary description of the heat budget, southern flank of Georges Bank, Spring–Summer, 1995: Part I. Surface heat flux, (abstract), *Eos, Trans. AGU*, 77(46), Fall Meet. Supp., F372, 1996.

Beardsley, R. C., A. G. Enriquez, C. A. Friehe, and C. A. Alessi, Intercomparison of aircraft and buoy measurements of wind and wind stress during SMILE, *J. Atmos. Oceanic Technol.*, 14, 969–977, 1997.

Berliand, M. E., and T. G. Berliand, Measurement of the effective radiation of the Earth with varying cloud amounts (in Russian), *Izv. Akad. Nauk SSSR, Ser. Geofiz.*, 1, 1952.

Brink, K. H., The near-surface dynamics of coastal upwelling, *Prog. Oceanogr.*, 12, 223–257, 1983.

Bryden, H. L., Horizontal advection of temperature for low-frequency motions, *Deep Sea Res.*, 23, 1165–1174, 1976.

Bryden, H. L., D. Halpern, and R. D. Pillsbury, Importance of eddy heat flux in a heat budget for Oregon coastal waters, *J. Geophys. Res.*, 85, 6649–6653, 1980.

Choppin, P. A., An examination of cup anemometer over-speeding, *Meteorol. Rundsch., 35*, 1–11, 1982.

Dean, J. P., and R. C. Beardsley, A vector-averaging wind recorder (VAWR) system for surface meteorological measurements in CODE (Coastal Ocean Dynamics Experiment), *Tech. Rep. WHOI-88-20*, 74 pp., Woods Hole Oceanogr. Inst., Woods Hole, Mass., 1988.

Dever, E. P., Wind-forced cross-shelf circulation on the northern California shelf, *J. Phys. Oceanogr., 27*, 1566–1580, 1997.

Dever, E. P., and S. J. Lentz, Heat and salt balances over the northern California shelf in winter and spring, *J. Geophys. Res., 99*, 16,001–16,017, 1994.

Dickey, T. D., D. V. Manov, D. A. Siegel, and R. A. Weller, Determination of longwave heat flux at the air–sea interface using measurements from buoy platforms. *J. Atmos. Oceanic Technol., 11*, 1057–1078, 1994.

Dorman, C. E., Evidence of Kelvin waves in California's marine layer and related eddy generation, *Mon. Weather Rev., 113*, 827–839, 1985.

Dorman, C. E., Possible role of gravity currents in northern California's coastal summer wind reversals, *J. Geophys. Res., 92*, 1497–1506, 1987.

Dorman, C. E., and C. D. Winant, Buoy observations of the atmosphere along the west coast of the United States, 1981–1990, *J. Geophys. Res., 100*, 16,029–16,044, 1995.

Dorman, C. E., A. G. Enriquez, and C. A. Friehe, Structure of the lower atmosphere over the northern California coast during winter, *Mon. Weather Rev., 123*, 2384–2404, 1995.

Enriquez, A. G., and C. A. Friehe, Bulk parameterization of momentum, heat, and moisture fluxes over a coastal upwelling area, *J. Geophys. Res., 102*, 5781–5798, 1997.

Fairall, C. W., and R. Markson, Mesoscale variations in surface stress, heat fluxes, and drag coefficient in the marginal ice zone during the 1983 Marginal Ice Zone Experiment, *J. Geophys. Res., 92*, 6921–6932, 1987.

Fairall, C., E. F. Bradley, D. P. Rogers, J. B. Edson, and G. S. Young, Bulk parameterization of air–sea fluxes for Tropical Ocean-Global Atmospheric Coupled Ocean–Atmospheric Response Experiment, *J. Geophys. Res., 101*, 3747–3764, 1996.

Federiuk, J., and J. S. Allen, Upwelling circulation on the Oregon continental shelf, II, Simulations and comparisons with observations, *J. Phys. Oceanogr., 25*, 1867–1889, 1995.

Friehe C. A., R. C. Beardsley, C. D. Winant, and J. P. Dean, Intercomparison of aircraft and surface buoy meteorological data during CODE 1, *J./,Atmos. Oceanic Technol., 1*, 79–86, 1984.

Fung, I. Y., D. E. Harrison, and A. A. Lacis, On the variability of the net longwave radiation at the ocean surface, *Rev. Geophys., 22*, 177–193, 1984.

Garratt, J. R., The stably stratified internal boundary layer for steady and diurnally varying offshore flow, *Boundary Layer Meteorol., 38*, 369–394, 1987.

Garratt, J. R., The internal boundary layer – A review, *Boundary Layer Meteorol., 50*, 171–203, 1990.

Garratt, J. R., and B. F. Ryan, The structure of the stably stratified internal boundary layer in offshore flow over the sea, *Boundary Layer Meteorol., 47*, 17–40, 1989.

Garratt, J. R., and M. Segal, On the contribution of atmospheric moisture to dew formation, *Boundary Layer Meteorol., 45*, 209–236, 1988.

Halpern, D., Structure of a coastal upwelling event observed off Oregon during July 1973, *Deep Sea Res., 23*, 495–508, 1976.

Halpern, D., J. R. Holbrook, and R. M. Reynolds, A compilation of wind, current, and temperature measurements: Oregon, July, and August 1973, *Tech. Rep. M74-73*, 190 pp., Univ. of Wash., Seattle, 1974.

Hamilton, G. D., NOAA Data Buoy Office programs, *Bull. Amer. Meteerol. Soc., 61*, 1012–1017, 1980.

Huyer, A., and P. M. Kosro, Mesoscale surveys over the shelf and slope in the upwelling region near Point Arena, California, *J. Geophys. Res., 92*, 1655–1681, 1987.

Irish, J. D., Moored temperature and conductivity observations, in CODE 2: Moored Array and Large-Scale Data Report, edited by R. Limeburner, *Tech. Rep. WHOI-85-35*, pp. 133–164, Woods Hole Oceanogr. Inst., Woods Hole, Mass., 1985.

Kelly, K. A., The influence of winds and topography on the sea surface temperature patterns over the northern California slope, *J. Geophys. Res., 90*, 11,783–11,798, 1985.

Large, W. G., and S. Pond, Open ocean momentum flux measurements in moderate to strong winds, *J. Phys. Oceanogr., 11*, 324–336, 1981.

Large, W. G., and S. Pond, Sensible and latent heat fluxes over the ocean, *J. Phys. Oceanogr., 12*, 464–482, 1982.

Large, W. G., J. Morzel, and G. B. Crawford, Accounting for surface wave distortion of the marine wind profile in low-level Ocean Storms wind measurements, *J. Phys. Oceanogr., 25*, 2959–2971, 1995.

Largier, J. L., B. A. Magnell, and C. D. Winant, Subtidal circulation over the northern California shelf, *J. Geophys. Res., 98*, 18,147–18,179, 1993.

Lentz, S. J., A description of the 1981 and 1982 spring transitions over the northern California shelf, *J. Geophys. Res., 92*, 1545–1567, 1987a.

Lentz, S. J., A heat budget for the northern California shelf during CODE 2, *J. Geophys. Res., 92*, 14,491–14,509, 1987b.

Lentz, S. J., The surface boundary layer in coastal upwelling regions, *J. Phys. Oceanogr., 22*, 1514–1539, 1992.

Lentz, S. J., and J. H. Trowbridge, The bottom boundary layer over the northern California shelf, *J. Phys. Oceanogr., 21*, 1186–1201, 1991.

Limeburner, R. (Ed.), CODE 2: Moored Array and Large-Scale Data Report, *Tech. Rep. WHOI-85-35*, 234 pp., Woods Hole Oceanogr. Inst., Woods Hole, Mass., 1985.

Limeburner, R., and R. C. Beardsley, CTD observations off northern California during the Shelf Mixed Layer Experiment (SMILE), November 1988, *Tech. Rep. WHOI-89-25*, 272 pp., Woods Hole Oceanogr. Inst., Woods Hole, Mass., 1989a.

Limeburner, R., and R. C. Beardsley, CTD observations off northern California during the Shelf Mixed Layer Experiment (SMILE), February–March 1989, *Tech. Rep. WHOI-89-41*, 218 pp., Woods Hole Oceanogr. Inst., Woods Hole, Mass., 1989b.

Limeburner, R., and R. C. Beardsley, CTD observations off northern California during the Shelf Mixed Layer Experiment (SMILE), May 1989, ,*Tech. Rep. WHOI-89-42*, 239 pp., Woods Hole Oceanogr. Inst., Woods Hole, Mass., 1989c.

List, R. J., Smithsonian Meteorological Tables, 527 pp., Smithsonian Inst. Press, Washington, D.C., 1984.

Liu, W. T., K. B. Katsaros, and J. A. Businger, Bulk parameterizations of the air–sea exchange of heat and water vapor including the molecular constraints on the sea surface, *J. Atmos. Sci., 36*, 1722–1735, 1979.

MacWhorter, M. A., and R. A. Weller, Error in measurements of incoming shortwave radiation made from ships and buoys, *J. Atmos. Oceanic Technol., 8*, 108–117, 1991.

Mooers, C.N.K., J. Fernandez-Partagas, and J. Price, Meteorological forcing fields of the New York Bight (first year's progress report). *Tech. Rep. TR76-8*, 151 pp., Univ. of Miami, Miami, Fla, 1976.

Mountain, D. G., G. A. Strout, and R. C. Beardsley, Sur-

face heat flux in the Gulf of Maine, *Deep Sea Res., 43*, GLOBEC Spec. Issue, 1533–1546, 1996.

Nelson, C. S., and D. M. Husby, Climatology of surface heat fluxes over the California Current region, *NOAA Tech. Rep. NMFS SSRF-763*, 155 pp., Natl. Oceanic and Atmos. Admin., Woods Hole, Mass., 1983.

Norment, H. G., Airflow about the WHOI VAWR cup anemometer, 178 pp., final report, Atmos. Sci. Assoc., Concord, Mass., 1992.

Payne, R. E., Albedo of the sea surface, *J. Atmos. Sci., 29*, 959–970, 1972.

Payne, R. E., Air temperature shield tests, *Tech. Rep. WHOI-87-40*, 22 pp., Woods Hole Oceanogr. Inst., Woods Hole, Mass., 1987.

Reed, R. K., An evaluation of formulas for estimating clear-sky insolation over the ocean, *Tech. Rep. ERL 352 - PMEL 26*, 25 pp., Natl. Oceanic and Atmos. Admin., Seattle, Wash., 1975.

Reed, R. K., On the estimation of net long-wave radiation from the oceans, *J. Geophys. Res., 81*, 5793–5794, 1976.

Reed, R. K., and D. Halpern, Radiation measurements off the Oregon coast: July/August 1973, *Tech. Rep. M74-18*, 51 pp., Univ. of Wash. Seattle, 1974.

Rogers, D. P., D. W. Johnson, and C. A. Friehe, The stable internal boundary layer over a coastal sea, I, Airborne measurements of the mean and turbulence structure, *J. Atmos. Sci., 52*, 667–683, 1995.

Rosenfeld, L. K. (Ed.), CODE 1: Moored Array and Large-Scale Data Report, *Tech. Rep. WHOI-83-23*, 185 pp., Woods Hole Oceanogr. Inst., Woods Hole, Mass., 1983.

Rosenfeld, L. K., Tidal band current variability over the northern California shelf, Ph.D. thesis, Mass. Inst. of Technol./Woods Hole Oceanogr. Inst., Woods Hole, Mass., 1987.

Rudnick, D. L., and R. E. Davis, Mass and heat budgets on the northern California shelf, *J. Geophys. Res., 93*, 14,013–14,024, 1988.

Samelson, R. M., Supercritical marine layer flow along a smoothly-varying coastline, *J. Atmos. Sci., 49*, 1571–1584, 1992.

Santala, M. J., Surface-referenced current meter measurements, Ph.D. thesis, Mass. Inst. of Technol./Woods Hole Oceanogr. Inst., Woods Hole, Mass., 1991.

Seckel, G. R., and F. H. Beaudry, The radiation from sun and sky over the north Pacific Ocean, (abstract), *Eos Trans. AGU, 54*, 1114 1973.

Send, U., R. C. Beardsley, and C. D. Winant, Relaxation from upwelling in the Coastal Ocean Dynamics Experiment, *J. Geophys. Res., 92*, 1683–1698, 1987.

Smith, S. D., Coefficients for sea surface wind stress, heat flux, and wind profiles as a function of wind stress and temperature, *J. Geophys. Res., 93*, 15,467–15,472, 1988.

Strub, P. T., and C. James, Atmospheric conditions during the spring and fall transitions in the coastal ocean off western United States, *J. Geophys. Res., 93*, 15,561–15,584, 1988.

Strub, P. T., J. S. Allen, A. Huyer, and R. L. Smith, Large-scale structure of the spring transition in the coastal ocean off North America, *J. Geophys. Res., 92*, 1527–1544, 1987.

Trask, R. P., J. P. Dean, J. R. Valdes, and C. D. Marquette, FASINEX (Frontal Air-Sea Interaction Experiment) moored instrumentation, *Tech. Rep. WHOI-89-3*, 60 pp., Woods Hole Oceanogr. Inst., Woods Hole, Mass., 1989.

Weller, R. A., and R. E. Davis, A vector measuring current meter, *Deep Sea Res., 27A*, 565–582, 1980.

Weller, R. A., D. L. Rudnick, R. E. Payne, J. P. Dean, N. J. Pennington, and R. P. Trask, Measuring near-surface meteorology over the ocean from an array of surface moorings in the Subtropical Convergence Zone, *J. Atmos. Oceanic Technol., 7*, 86–103, 1990.

Winant, C. D., C. E. Dorman, C. A. Friehe, and R. C. Beardsley, The marine layer off northern California: An example of supercritical channel flow, *J. Atmos. Sci., 45*, 3588–3605, 1988.

Zemba, J., and C. A. Friehe, The marine atmospheric boundary layer jet in the Coastal Ocean Dynamics Experiment, *J. Geophys. Res., 92*, 1489–1496, 1987.

R. C. Beardsley, J. P. Dean, and S. J. Lentz, Physical Oceanography Department, Mail Stop 21, Woods Hole Oceanographic Institution, Woods Hole, MA 02543-1541.

E. P. Dever, Center for Coastal Studies, Scripps Institution of Oceanography, University of California, San Diego, La Jolla, CA 92093-0209.